Development of the low bandgap materials Ge:H and GeSn:H by plasma enhanced chemical vapor deposition

by

Koos Roodenburg

to obtain the degree of Master of Science

at the Delft University of Technology,

to be defended publicly on Thursday November 18, 2021 at 02:00 PM.

Student number:	4476557	
Project duration:	October 1, 2020 – November 18, 2021	
Thesis committee:	Prof. dr. Arno Smets	TU Delft, supervisor
	Prof. dr. Ivan Gordon	TU Delft
	Dr. ir. Aditya Shekhar	TU Delft
	Ir. Thierry de Vrijer	TU Delft, daily supervisor

Acknowledgements

By completing this Thesis I graduate the Master of Science program 'Sustainable Energy Technology' at the Delft University of Technology. During this program, I followed various interesting courses based on the generation and storage of energy in a renewable way. The final project was a unique opportunity for me to gain experience in developing photovoltaic technologies. I helped in the development of low bandgap materials which can be used later on in solar cells to improve their efficiency. Such developments can accelerate the energy transition enormously. Therefore I am grateful to have been able to do this project and would like to thank everyone who helped me.

As I was not able to achieve this result by myself, I also would like to thank several people in person. First of all, I would like to thank my two supervisors Prof. dr. Arno Smets and Ir. Thierry de Vrijer. They guided me throughout the project and when I had a question I could ask them. As daily supervisor, Thierry helped me a lot by regularly sharing his ideas and knowledge on the subject with me. Also Arno's feedback was very helpful. Their passion and enthusiasm are contagious, which makes me want to work on solar energy topics in the future.

Furthermore, I would like to thank the technicians of the Else Kooi Lab: Martijn Tijssen, Stefaan Heirman and Daragh O'Connor. They ensured me that the equipment worked in these difficult corona times in where also many relocations took place. Special thanks goes to Martijn, he was always quickly on the spot when there was an issue with the CASCADE and he made it possible to process Ge:H and GeSn:H layers.

I also want to thank my fellow students Ir. Julian van Dingen and Ir. Paul Roelandschap. They showed me how to use the CASCADE in the correct way and taught me how to perform the measurements to characterize the deposited layers. They were also there when I had a question about the practical part of the project. My last words of thanks go to Thijs Blackstone and Federica Saitta, who helped me to process additional GeSn:H layers at the end of my thesis.

Koos Roodenburg
Delft, August 2021

Abstract

The development in solar cells began with wafer based cells, also called the first generation photovoltaic technology. Most of these wafer based cells were made of crystalline silicon. As a crystalline silicon cell must be relatively thick to absorb most of the incoming energy, the second generation (thin film solar cells) was introduced. In the third generation the focus is more on achieving high efficiencies at low production costs. A way to achieve higher efficiencies is by the use of multi-junction devices. In such devices, different sub cells are stacked onto each other and in this way a larger part of the solar spectrum can be utilized. Also the spectral mismatch losses will be minimized. Moreover, the fabrication costs of multi-junction devices can significantly be reduced by using a cheap processing technique, like plasma enhanced chemical vapor deposition (PECVD).

When germanium and germanium-tin are passivated by hydrogen atoms, Ge:H has its theoretical bandgap in the 0.9-1.1eV range and GeSn:H its bandgap in the 0.6-1.0eV range. The use of such low bandgap materials facilitates absorption of photons in the infrared spectrum, what reduces the non-absorption losses. Their low bandgaps make them perfect candidates to act as the absorber material in a bottom cell in a multi-junction device. Both materials can also be processed by PECVD.

In this thesis about 100 Ge(Sn):H films were PECVD processed in the CASCADE reactor located in the Else Kooi Lab. The objective was optimizing the plasma conditions to obtain device quality thin films. A device quality bottom cell material must fulfil some requirements, like having a low bandgap, being intrinsic and having a high photo response. The influence of various deposition parameters was investigated to characterize their effect on the material properties.

It was found that a densification of Ge(Sn):H generally lead to lower bandgap energies. Densification of these materials can be caused by increasing the substrate temperature (in the 250-300°C range). Next to this, a decrease in hydrogen dilution (in the 100-400 range) also leads to lower bandgap energies for the amorphous Ge(Sn):H films. By combining a substrate temperature of 290°C with a hydrogen dilution of 100, promising a-Ge:H films were processed containing refractive indexes above 5.3, optical bandgap energies below 1.1eV, activation energies above 330meV and dark conductivities below $5 \cdot 10^{-4}\ \Omega^{-1}cm^{-1}$. The material properties of the processed a-GeSn:H films were even closer to a device quality bottom cell material. Nevertheless, processing device quality GeSn:H layers remains challenging. Adding relatively large amounts of tetramethyltin (TMT) into the plasma chamber led to clusters of tin and significant oxygen and carbon concentrations throughout the layer. Managing the atomic carbon, oxygen, germanium and tin fractions could be crucial in obtaining device quality bottom cell absorber layers based on Ge(Sn):H in the future.

Table of Contents

1 Introduction

Power plugs and sockets have become essential elements in our everyday lives. Electricity is required to fulfill almost all our needs, such as transportation, lighting our houses and charging our phones. Due to technological progress combined with population growth in the last decades, the total energy demand drastically increased [1]. As an example, the world total final consumption was 73 PWh in 1990 and 116 PWh in 2018 [2]. Such large amounts of consumed energy automatically indicate that at least an equal amount is produced. In 1990, the electrical energy consumption was mainly (88%) generated out of fossil fuels, like coal, crude oil and natural gas [3]. Almost 30 years later, fossil fuels still are the main sources of our electrical energy production. Nevertheless, the share of renewables grew during this period, as shown in figure 1. This is the result of a global energy transition, which started to reduce global warming [4].

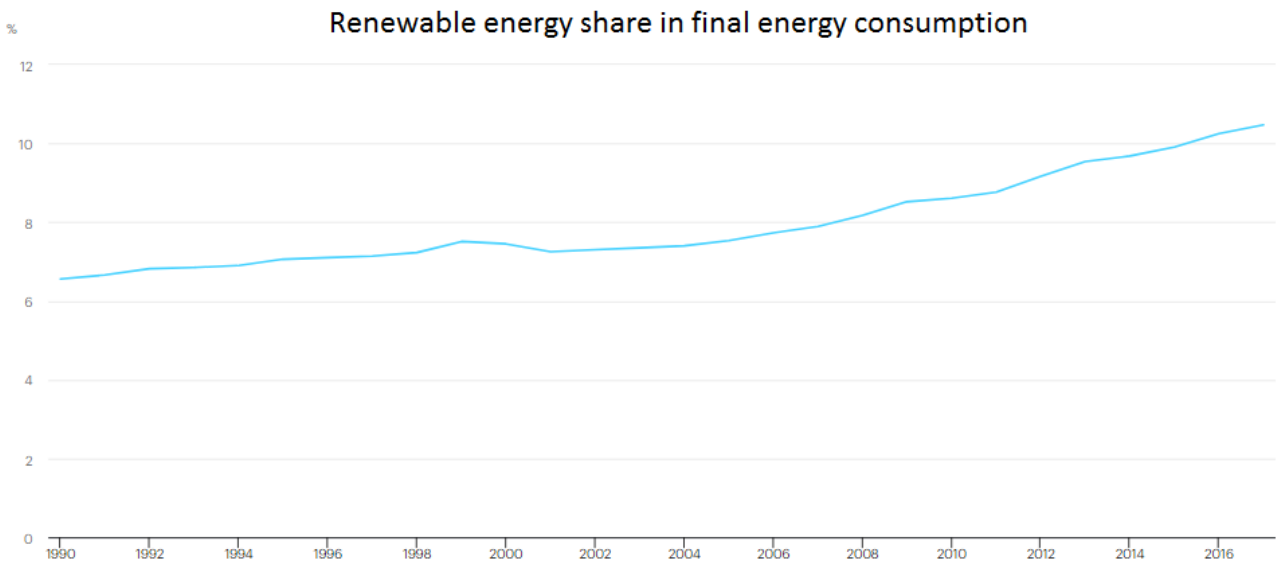

Figure 1: Share of renewable energy in total final consumption worldwide [5].

Looking at the reasons for a global energy transition in more detail, the arguments to replace fossil fuels by renewables are largely based on economic and climate aspects. The usage of fossil fuels began in the industrial revolution, which started in the 18th century [6]. During the industrial revolution the transition was made from human labor to machinery. The mining of fossil fuels was relatively simple and therefore fossil fuels were used a lot; the world economy depended upon it. As the extraction is location dependent, countries with large fossil fuels reserves gained enormous political and economic power. In 1973 the Arabic countries used their power to increase the oil price exponentially [7], which led to an oil crisis and the Western world started thinking about new energy sources. A lot of research was done into renewable alternatives, especially because fossil fuels became scarcer in the West [8]. It did not lead to a large energy turnaround yet, but the share of renewable energy grew in the years after. Another reason for this was the growing public attention for global warming. On the long term global warming can lead to a significant sea level rise and to the extinction of plants and animal species [9].

The energy transition from fossil to renewable energy sources will be crucial in reducing global warming. The size of this reduction is described in the Paris Agreement from 2015. This is an agreement between 197 countries worldwide in which multiple climate goals are noted. The most important goal is that the global average temperature may not exceed 2°C above pre-industrial levels [10]. Another goal of the EU is to become climate neutral in 2050 [11]. As global warming depends on the amount of emitted greenhouse gasses by burning fossil fuels, the use of fossil fuels has to decrease drastically to reach all these goals. A renewable alternative having a high potential to replace fossil fuel energy generation is solar energy. In fact, the amount of solar energy reaching the Earth's surface is large enough to meet the total energy consumption worldwide many times over [12]. Therefore, the development in photovoltaic (PV) technologies can be decisive in achieving the climate goals. For a better understanding of the developments, first the working principle of a solar cell will be explained.

1.1 Working principle of a solar cell

A solar cell is an advanced semiconductor device and its working principle is based on the photovoltaic effect as it converts electromagnetic radiation into a voltage difference and current [13]. The sun is a source emitting electromagnetic radiation in the form of visible light, infrared and ultra-violet [14]. During the conversion, the following steps are taken by the solar cell: absorption of light, generation of charge carriers, separation of charge carriers and collection of charge carriers [15]. All steps will be explained in this section.

1.1.1 Absorption of light

The sun emits electromagnetic radiation in the wavelength range from 250 nm to roughly 2500 nm [16]. Actually, higher wavelengths electromagnetic radiation are emitted as well, but the intensity for these large wavelengths is almost negligible. The electromagnetic radiation spectrum is divided into groups based on the wavelength, as shown in figure 2. For example, visible light is the radiation containing wavelengths between 380 nm and 760 nm. Higher wavelengths lead to infrared radiation or radio waves and smaller wavelengths to ultra-violet radiation, X-rays or gamma rays.

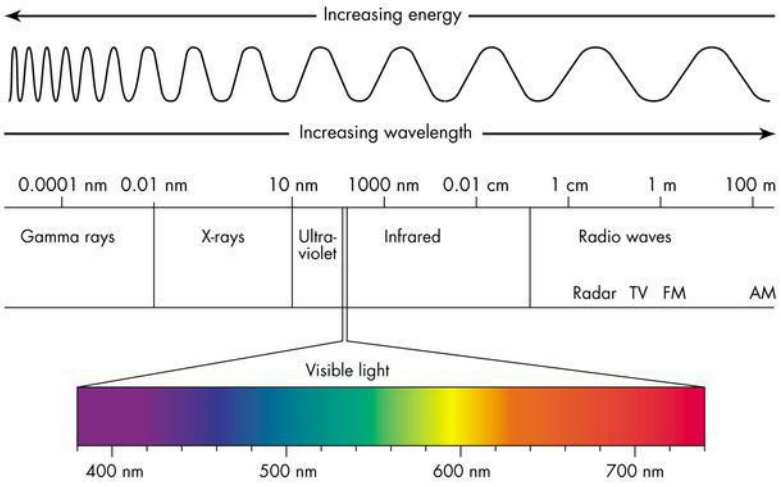

Figure 2: Diagram of the electromagnetic spectrum [17] .

Next to a wave behavior, light also behaves as a particle. Therefore the behavior of light is called wave-particle duality [15]. Its explanation is that light consists of very tiny particles, called photons, containing all a small amount of energy and their energy level depends on the wavelength of light. In equation 1, the energy of a photon is given. Where h is Planck's constant, c the speed of light and λ the wavelength of the electromagnetic waves.

$$E_{ph} = \frac{hc}{\lambda} \tag{1}$$

From equation 1, lower wavelengths of light corresponds to higher photon energies. However, the total energy received by the Earth's surface also depends on the photon distribution (the amount of photons containing a particular energy level) of incident electromagnetic radiation. Therefore the spectral irradiance is an important property, which is the power received by the Earth's surface per square meter per wavelength (W/m²nm). In figure 3, the solar irradiance incident on Earth is plotted against the wavelength.

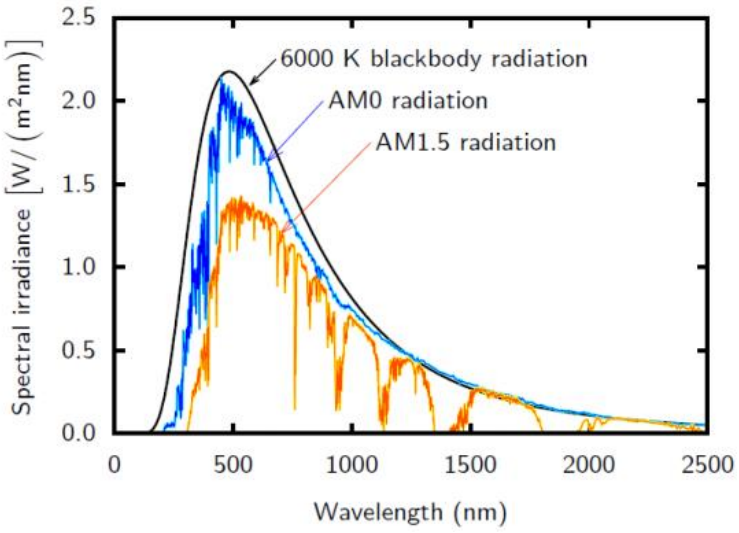

Figure 3: Spectral irradiance for three types of solar spectra: the blackbody radiation, the AM0 radiation and the AM1.5 radiation [18].

Figure 3 shows the spectral irradiance for three types of solar spectra. The blackbody radiation spectrum is based on the blackbody concept where the sun is a perfect blackbody, meaning that it absorbs all radiation incident on it and its reflectivity is equal to zero [15]. Next to this, the spectral irradiance of the AM0 and AM1.5 spectra are also plotted. The number behind air mass (AM) is a notation for the travel distance of the sunlight through the atmosphere. To be more concrete, it is the ratio of the path length through the atmosphere to the path length through the atmosphere when the incident light is normal to the Earth's surface [19]. The AM1.5 spectral irradiance is lower than the AM0 irradiance as the sunlight travels a longer distance through the atmosphere in where it can attenuate. Usually the AM1.5 spectrum is used to illuminate the solar cells for testing. Other standard test conditions (STC) are a cell temperature of 25°C and an irradiance of 1,000 W/m^2 (area under AM1.5 spectrum) [15].

1.1.2 Generation of charge carriers

Let us now take a closer look the solar cell itself. As mentioned earlier, a solar cell is made of a semiconductor material. A semiconductor lies between an insulator and a conductor based on its conductivity. The physical explanation for this has to do with the bandgap size, which is illustrated in figure 4. The energy on the y-axis gives the energy level of electrons inside the specific material. Electrons can only contain energy levels within the valence or the conduction band. Within the bandgap, also called the forbidden gap, no possible energy state exist. A valence electron (electron located in the outer shell of an atom that is able to form a covalent bond with another atom [15]) containing an energy level within the valence band can be excited when it receives sufficient external energy. After excitation it acts as a free electron containing an energy level located in the conduction band. The amount of free electrons moving through the lattice determines the conductivity of a material.

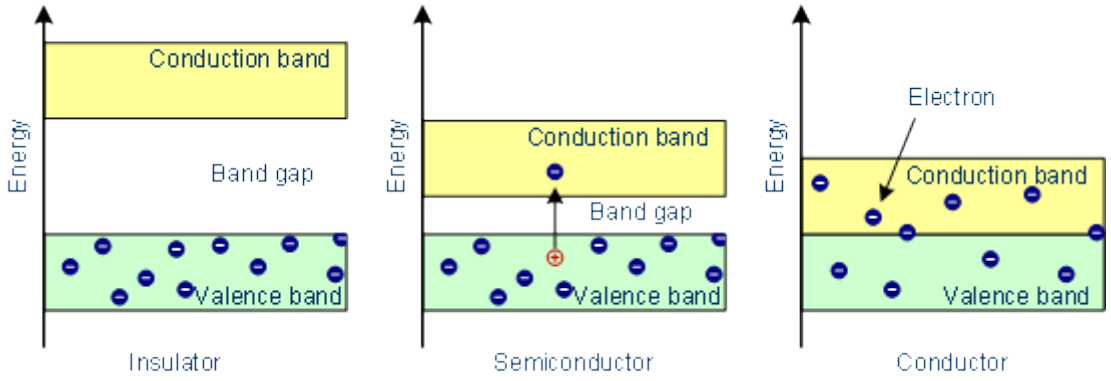

Figure 4: Band diagrams for insulators, semiconductors and conductors [20].

From figure 4, a conductor does not have a bandgap between the conduction and valance band. Therefore the valence electrons inside a conductor can already be excited when a relatively small external energy is added. Insulators, however, do have large bandgaps. Then the valence electrons have to bridge a large energy difference for excitation, resulting in a very low density of conducting electrons. A semiconductor is a special type of insulator as its bandgap is relatively small. This makes it possible for the electrons to be excited from the valence to the conduction band by a relativity small amount of external energy. For solar cells this external energy is provided by solar radiation. The photon energy is not large enough to excite the electrons from the valence to the conduction band in an insulator. Therefore insulators cannot be used in solar cells.

The schematic representations in figure 4 are very simplistic. In reality, the bandgap energy is not the only important aspect in the excitation of an electron from the valence to the conduction band. The electrons could also need a change in momentum [15], which can be better explained when we introduce the k-vector on the x-axis, as shown in figure 5. Now the valence and conduction bands are not flat lines anymore. When the highest energy level in the valance band and the lowest energy level in the conduction band are located at the same k-vector, the bandgap is called a direct bandgap. For direct bandgap semiconductors, the electrons only have to overcome the bandgap energy to excite to the conduction band. For indirect bandgaps this is different. Then the electrons also need a change in momentum for excitation.

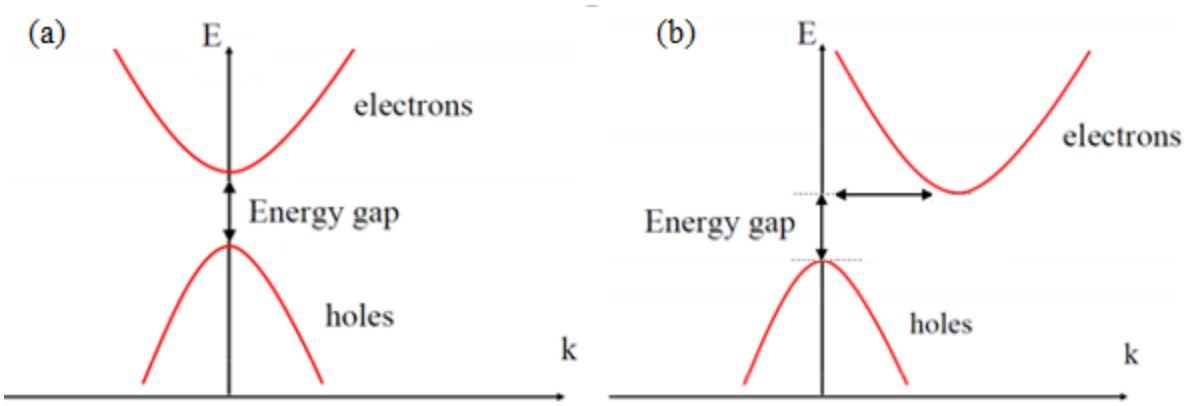

Figure 5: Schematic representations of a direct (a) and an indirect (b) bandgap [21].

In the valance band a hole is created when an electron is excited to the conduction band. A hole can be seen as a positively charged particle (positive elementary charged) as it is the absence of a negative charged electron [22]. Both the excited electron and the hole are able to move freely through the lattice. This is the result of the broken covalent bonds what took place during the excitation.

Looking to the atomic structure in more detail; germanium, silicon and tin atoms do all have four valence electrons as they are Group IV elements. Therefore these atoms can form bonds with four other atoms. The same principle holds for their neighboring atoms and their neighboring atoms, so a whole atomic network can be made [23]. Such a network can be crystalline or amorphous structured, as shown in figure 6. In a crystalline network, the bond angles and distance between the atoms are the same over the whole network. In an amorphous network, however, there is no pattern visible. From figure 6, some atoms in the amorphous network are not able to make covalent bonds due to the structural disorder. The disconnected bonds are called dangling bonds and can act as defect states within the bandgap. To reduce the defect density, dangling bonds can be passivated by hydrogen atoms. This is indicated by ':H' in the abbreviations Ge:H and GeSn:H [15].

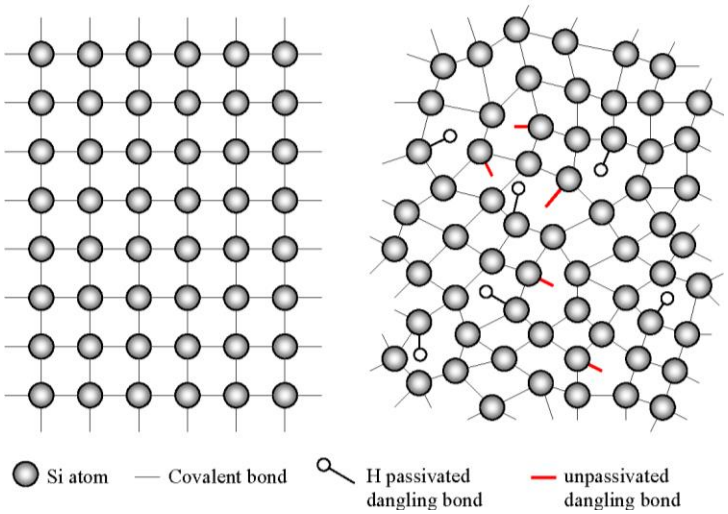

Figure 6: Schematic representations of a crystalline (left) and an amorphous (right) atomic structure [23].

1.1.3 Separation and collection of charge carriers

After excitation of an electron to the conduction band, the free electrons and holes need to be separated immediately. Otherwise an electron eventually falls back into a hole in the valence band, called recombination. The separation of the free electrons and holes is usually done by manipulating the electron and hole concentrations, called doping. In doped semiconductors some atoms are replaced by atoms of another semiconductor group and thus having a different amount of valence electrons. As an example, when a silicon atom (containing four valence electrons) will be replaced by a phosphorus atom (containing five valence electrons), one valence electron cannot take part in the atomic network and is therefore weakly bound. This bond can easily break and then a free electron moves through the lattice. When this happens, the phosphorus atom is called a donor as it 'donates' an electron. The other way around is possible as well. When a boron atom (containing three valence electrons) was used instead of a phosphorus one, this atom can easily 'accept' an electron and is called an acceptor [15].

When the concentration of one type of charge carrier is dominant, we call such semiconductors n-type or p-type. In an n-type semiconductor, the free electron concentration is larger than the concentration of holes. For a p-type semiconductor this is the other way around. A semiconductor is called intrinsic when the electron and hole concentrations are equal. For intrinsic semiconductors the average electron energy in the material, called the Fermi energy level, lies in the middle of the bandgap. For the n-type and p-type semiconductors the Fermi energy level lies respectively closer to the conduction band or valance band edge.

To separate the electrons and holes, an n-type semiconductor and a p-type semiconductor are brought together, as shown in figure 7. The large difference in electron and hole concentrations between both semiconductors causes a diffusion current of holes from the p-type to the n-type semiconductor and a diffusion current of electrons from the n-type to the p-type semiconductor. Due to the diffusions, the region close to the PN-junction will be depleted by charge carriers and is therefore called the space charge region or the depletion region. The depletion of electrons and holes in the depletion region results in a space charge creating an electric field [22]. This electric field arises in the opposite direction to the diffusion currents. In this way the net current becomes zero and the two forces cancel each other out [15]. Then the electrons and holes cannot move any further and are separated. Adding electrical contacts allows the electrons to travel through an external circuit.

In defect rich materials the diffusion length/carrier lifetime is too short to move the charge carriers to the depletion region. For this type materials p-i-n junctions are used. Then an intrinsic semiconductor is placed between a thin n-type and p-type semiconductor. An electric field is then created by the presence of these semiconductors, leading to a drift current as main transport mechanism for the charge carriers [15].

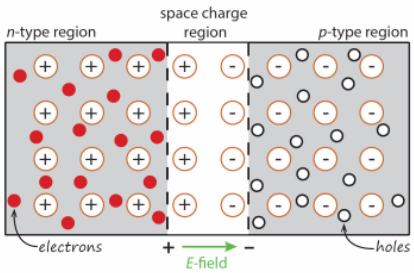

Figure 7: Schematic representation of a PN-junction [15].

1.2 Developments in PV technology

This section describes the first generations of solar cells together with their (dis)advantages. This section will also zoom in on smaller developments related to the topic of this thesis.

1.2.1 The first generations

The development in solar cells began with wafer based cells, also called the first generation PV technology [24]. Most of these wafer based cells were made of crystalline silicon (c-Si). Silicon is a relative abundant material, what makes it a cheap material with respect to elements from groups III-VI. On the other hand, a c-Si cell must be thick to absorb most of the incoming energy as it has a low absorption coefficient. This makes the production of c-Si solar cells still expensive compared to thin film devices [15]. For this reason an alternative was introduced: the thin-film solar cells. These second generation solar cells can be made 100 times thinner than wafer based cells [25]. Nevertheless, the efficiencies of thin-film solar cells are lower and the price of wafer based cells dropped when the thin film cells were introduced. Therefore the market share of wafer based solar cells is still much higher than the market share of thin-film solar cells [26]. In the third generation the focus is more on achieving high efficiencies at low production costs [27]. Most of the third generation concepts, such as splitting or combining photons to minimize energy losses, are still in the experimental phase.

1.2.2 Multi-junction devices

The energy production by PV technologies grew exponentially in the last few years. To be concrete, the electricity generation by PV technologies was increased from 32,000 GWh in 2010 to 554,000 GWh eight years later [28]. Nevertheless, a lot of research is still being done to achieve higher conversion efficiencies. The two main losses in photovoltaic devices are based on non-absorption and thermalization. These two losses are both spectral mismatch related, meaning there is a mismatch between the energy level of the incident photons and the bandgap energy of the semiconductor material [15]. Both losses are schematically illustrated in figure 8.

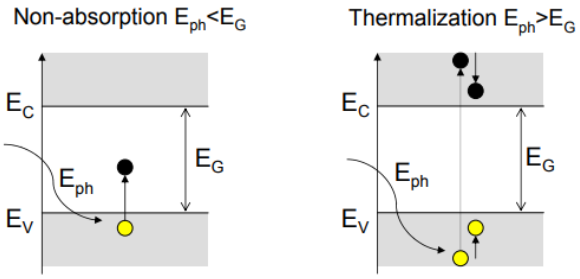

Figure 8: Schematic representation of non-absorption and thermalization [15].

Non-absorption occurs when the energy of the photon is lower than the bandgap energy. Then the electron cannot be excited to the conduction band and the energy of the photon is not used. In contrast to non-absorption, thermalization occurs when the photon energy is higher than the bandgap energy. The electron excites to the conduction band, but its energy level falls back to the lowest energy level within the conduction band. All excess energy is released as heat [15].

According to the Shockley-Queisser limit, a single-junction solar cell does have a maximum theoretical efficiency of 33.1% [29]. The loss in efficiency is largely based on the two main losses described on the previous page. The size of these losses depends on the semiconductor material used in the solar cell, because each semiconductor material has its own characteristic bandgap energy. As an example, silicon (1.12 eV) has a lower bandgap energy than the combination GaInP (1.86 eV). Therefore silicon can absorb photons containing a minimum energy level of 1.12 eV, while GaInP only absorbs photons with energy levels above 1.86 eV. On the other hand, a silicon solar cell does also have higher thermalization losses compared to GaInP solar cells [15].

The efficiency of a solar cell can be improved by using more than one semiconductor for absorption, called multi-junction devices. In such devices, different sub cells are stacked onto each other. In a multi-junction solar cell, the semiconductor having the highest bandgap is positioned first in reference to the incident light and the semiconductor having the lowest bandgap is positioned last. The cells in the middle are also positioned based on the respective bandgap energies of the absorber materials. Incident photons containing high energy levels will be absorbed by the top cell, while photons containing lower energies will be absorbed by one of the middle or bottom cells. In this way a larger part of the solar spectrum can be utilized and both spectral mismatch losses are minimized. In figure 9 this multi-junction concept is illustrated.

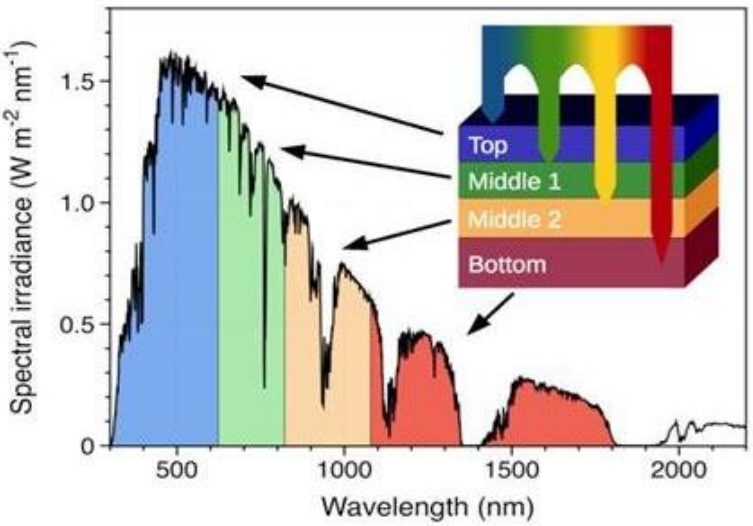

Figure 9: The different cells in a multi-junction device all utilize another part of the solar spectrum [22].

A disadvantage of multi-junction devices relative to single-junction devices is that the fabrication process consists of multiple (extra) steps and more materials have to be used. As a result, multi-junctions are usually more expensive than single-junctions. A way to reduce the fabrication costs is to make use of cheap processing techniques, like plasma enhanced chemical vapor deposition (PECVD). By using the PECVD technique, a material can be deposited without using high temperatures (range 200-300°C), what reduces the processing costs significantly [22] [23].

1.2.3 Ge:H and GeSn:H as bottom cell candidates

In this work is focused on the development of the materials Ge:H and GeSn:H, which can both be processed by PECVD. Their characteristics and the motivation to develop these materials are described below.

Germanium and tin are both group IV elements and have atom number 32 and 50 in the periodic table, respectively. Both elements, being from group IV, can form covalent bonds with four neighboring atoms. When germanium and germanium-tin are passivated by hydrogen atoms, Ge:H has its bandgap in the 0.9-1.1eV range and GeSn:H its bandgap in the 0.6-1.0eV range. In figure 10 this range is shown in an AM1.5 spectrum plot. Compared with silicon (1.12 eV), the theoretical bandgap of Ge(Sn):H is significantly lower and can therefore be used to collect photon energies a silicon solar cell cannot utilize.

alloy	Band gap (eV)
a-GeSn:H	0.6-1.0
c-Si	1.1
nc-Si:H	1.1-1.3
a-SiGe:H	1.4-1.6
a-Si:H	1.6-1.8
a-SiOx:H	>2.0

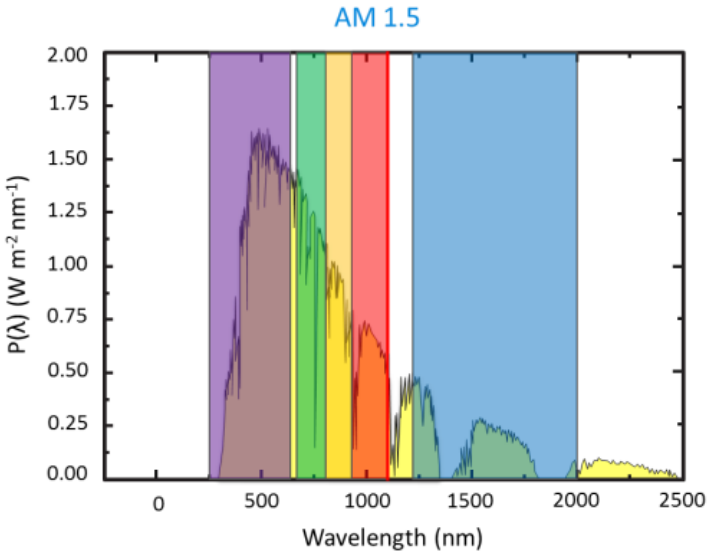

Figure 10: Bandgap ranges for some group IV alloys [30].

Using such low bandgap materials facilitates absorption of photons in the infrared spectrum, what can significantly reduce the non-absorption losses. As low bandgaps will lead to enormous thermalization losses when high energy photons are incident on it, it is not preferred to use Ge(Sn):H in a single-junction cell. Their low bandgaps make them perfect candidates to act as absorber materials in a bottom cell in multi-junction devices. And due to the significant amount of photons in the infrared spectrum, a bottom cell made of Ge(Sn):H will likely not be current limiting or limit the fill factor [30].

1.3 Aim and outline of the thesis

The aim of this project is to develop the semiconductor materials Ge:H and GeSn:H by using the plasma enhanced chemical vapor deposition (PECVD) technique. Development of a material in this case means optimizing the plasma settings to deposit device quality thin layers/films. Integrating device quality PECVD processed materials in multi-junction devices could lead to an efficiency boost against low cost. The main question of this thesis is as follows:

How can the plasma settings be optimized to obtain device quality Ge(Sn):H films processed by the PECVD technique?

Device quality bottom cell materials must fulfil the following requirements: they must have a low bandgap energy to absorb photons in the higher wavelength range, they should be intrinsic for the use in a p-i-n junction and their photo response must be high enough for obtaining a sufficient current density. This can only be achieved when the material is stable (no interaction with other elements that influence the material badly). The sub-questions of this thesis are therefore:

1) ***How to obtain low bandgaps for Ge(Sn):H films?***
2) ***How to obtain intrinsic Ge(Sn):H films?***
3) ***How to obtain a sufficient photo response for Ge(Sn):H films?***

Earlier research [22] [23] [31] into Ge:H films deposited with the PECVD technique showed a stability improvement of the material when higher substrate temperatures were used. Therefore three temperature series were processed in this thesis to understand the effect of substrate temperature on the material properties of Ge:H in more detail. After request of INTEL and Ghent University, also Ge:H series with different thicknesses and hydrogen dilutions were processed. For processing suitable GeSn:H layers, almost the same plasma settings were used as for our best Ge:H layers, except the ones regulating the tin supply. The settings influencing the tin supply have been investigated extensively by processing a deposition series for each setting. Additionally, also other plasma parameters were varied to characterize their effect on GeSn:H.

In this thesis the materials were deposited by the CASCADE (Cascaded Arc Solar Cell Apparatus Delft Eindhoven) reactor located in cleanroom 10,000 of the Else Kooi Lab in Delft, which uses the PECVD technique to deposit materials. Multiple layers with different plasma settings were processed in the CASCADE and later characterized in several labs located on the university campus in Delft. The characterization process consists of several measurements to find and analyze interesting material properties.

The outline of this report is as follows. Chapters 2 and 3 are theoretical chapters containing information about the fabrication and characterization processes. Chapters 4 and 5 present the experimental results for the Ge:H and GeSn:H layers processed in this work and chapter 6 provides the conclusion and recommendations for future research.

2 Fabrication process

This chapter describes the fabrication processes to produce the thin Ge:H and GeSn:H layers. These films were grown on both a Corning XG glass substrate and a Siegert monocrystalline silicon wafer. These two substrates were chemically cleaned before the deposition process started. Their cleaning processes are described in section 4.1. PECVD was used to process the Ge(Sn):H films, as described in section 4.2. In this process an electric field ionizes the precursor gasses present in the deposition chamber, what creates a plasma. These gasses contain the selected materials that must grow on the substrates. When the deposition was finished, metal contacts were evaporated onto the deposition side of the glass substrates to measure the material properties. This process is described in section 4.3. In section 4.4 the last fabrication step, annealing, will be explained.

2.1 Cleaning

The cleaning of the Corning Glass XG glass substrates was done in an ultrasonic bath filled with water. Inside this water bath two smaller baths were located. One of them is filled with acetone and the other with isopropanol (IPA). The glass substrates will first be placed in the acetone bath for 10 minutes and later on in the isopropanol bath for another 10 minutes. During these 20 minutes the ultrasonic bath was switched on. Then sonic waves were generated to create bubbles in the solvents, which aid in the removal of contaminants from the substrate. Contaminations could possibly influence the growth of the films. After each cleaning, the substrates were blow dried using a nitrogen air gun.

The Siegert 100mm diameter monocrystalline silicon wafers were cleaned in another way. First the wafers were dipped for 4 minutes into a bath filled with 0.5% HF solution to remove the oxide layer from the wafer. During the last minute isopropanol was added to the solution. After these 4 minutes, the wafers were rinsed and dried by using the Marangoni effect. Then also DI water is added into the bath for 4 minutes. As the bath is small in volume, the 0.5% HF solution on top flows out of the bath. Now the bath only contains a mixture of DI water and isopropanol. As the isopropanol has a low surface tension, the water will slide off the wafer when the wafer slowly rises out of the bath.

When the cleaning process of both the glass substrate and the silicon wafer are finished, they will be cut/broken into smaller pieces (2.5cm x 10cm rectangles for glass and quart or half wafers for silicon).

2.2 Plasma enhanced chemical vapor deposition

The films were grown in the CASCADE (Cascaded Arc Solar Cell Apparatus Delft Eindhoven) reactor located in cleanroom 10,000 of the Else Kooi Lab in Delft. The CASCADE reactor uses the radio frequency plasma enhanced chemical vapor deposition technique (RF-PECVD) to deposit very thin material layers in the nanometer range. The CASCADE reactor includes a plasma chamber (RF chamber/reaction chamber) in which the deposition takes place and a load lock in where the substrate holder (containing the glass and silicon substrates) can be placed. Between both rooms there is a partition so that the reaction chamber will never be affected by air particles or dust.

When the substrate holder is placed inside the load lock, a gripping arm rotates the substrate holder in such a way that the glass and silicon are facing downwards. Then the gripping arm moves the substrate holder inside the reaction chamber directly below the upper electrode, as shown in figure 11. The upper electrode is grounded and the lower electrode is connected to a RF generator. Both electrodes are circular having a diameter of 16cm. The RF generator creates an alternating voltage leading to an oscillating electric field between the two electrodes.

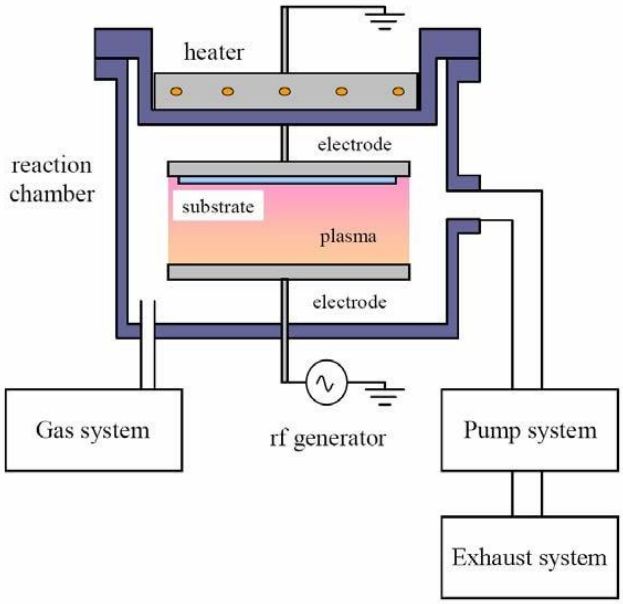

Figure 11: Schematic representation of the inside of the reaction chamber together with the pump and gas systems [15].

The deposition process starts by introducing a laminar gas flow from the gas system to the reaction chamber. This gas flow consists of a mixture of precursor gasses depending on the type of material that has to be made. As an example, a mixture of hydrogen (H_2) and germane (GeH_4) gasses was used to deposit Ge:H layers and a mixture of H_2, GeH_4 and tetramethyltin/TMT ($C_4H_{12}Sn$) gasses was used to deposit GeSn:H layers. The precursor gasses will be ionized inside the reaction chamber by the presence of the electric field between the two electrodes. The excited electrons are able to ionize other atoms in the gas as well. A plasma is formed when a sufficient number of gas atoms are ionized [32]. Within the plasma there are electrons, ions, neutral atoms and free radicals present by the dissociation of the gasses [33]. The free radicals attach to the substrate when they come into contact with it and will form the deposited layer. In the equations below [34], the most common plasma reactions shown to create the free radicals out of germane and hydrogen gasses.

$$e^- + GeH_4 \leftrightarrow GeH_3 + H^+ \quad (2)$$

$$e^- + GeH_3 \leftrightarrow GeH_2 + H^+ \quad (3)$$

$$H^+ + GeH_4 \leftrightarrow GeH_3 + H_2 \quad (4)$$

The growth of the deposited layer is a constant process as there are continuous precursor gas flows during the whole deposition. However, the flow of TMT is regulated in a different way. TMT is a liquid at room temperature and is therefore vaporized in a bubbler to 74°C. Its flow was controlled by an atomic layer deposition (ALD) valve located between the bubbler and the reaction chamber. This valve can either be open or closed and goes in cycles. One cycle consists of an open time (in ms) plus a close time (in ms) and the amount of cycles depends on the time of the deposition. In this thesis the duty cycle is used to express the flow rate of TMT, which is the close time divided by the open time. For some depositions also a helium (He) carrier gas was used to improve the TMT flow. A carrier gas can help to distribute the TMT more uniformly in the reaction chamber.

In this thesis, multiple parameters were varied to obtain the most suitable Ge:H and GeSn:H layers. The varied parameters were the substrate temperature (T_s), the pressure inside the reaction chamber (p), the electrode distance (e_d), the power of the RF generator (P_{RF}) and the gas flows of hydrogen (F_{H2}), germane (F_{GeH4}), TMT (duty cycle) and helium (F_{He}). The thickness of the layers depends on the deposition time (t).

2.3 Metal evaporation

After depositing the films in the CASCADE, metal contacts on top of the layers are needed to perform the electrical measurements. These metal contacts were deposited by the PROVAC 500 machine located in cleanroom 10,000 of the Else Kooi Lab. A schematic representation of its inside is shown in figure 12.

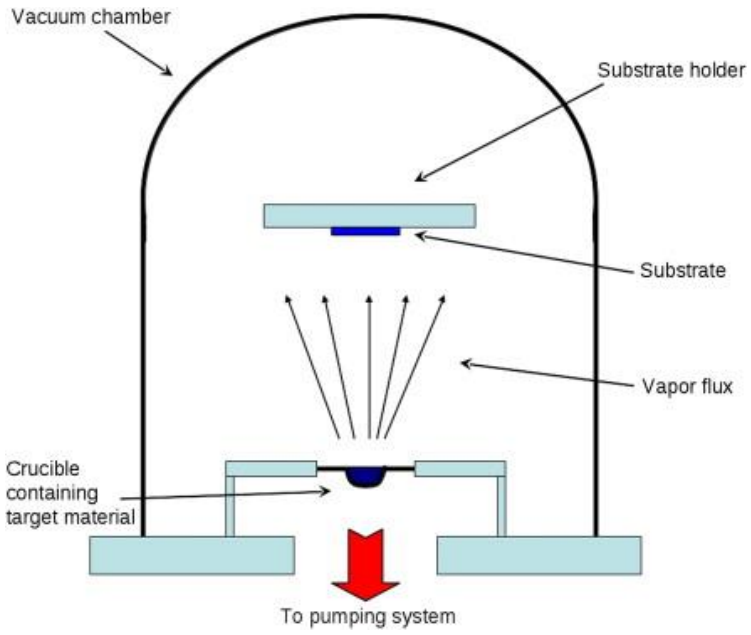

Figure 12: Schematic representation of the inside of the Provac 500 [35].

The working principle of the PROVAC 500 is based on evaporation and condensation of a target material. In this thesis, aluminum was used as target material. First some aluminum pieces were placed inside the crucible and the films (on glass) were clamped in the substrate holder in such a way that the deposition side is facing downwards. A mask containing the desired pattern is placed under the layers to deposit the aluminum contacts in the correct dimensions. After pumping down the chamber, the aluminum pieces were heated up to their melting point by focusing a high intensity electron beam on them. The aluminum gas particles will rise inside the vacuum chamber until they reach the films. There the aluminum will condense to a solid state and the metal contacts are formed.

During the aluminum deposition the substrate holder rotates at 10rpm to get a uniform material. The deposition time is set to obtain contact heights of 500nm. The pattern of the aluminum contacts is as follows: there are two rectangular bars (20mm x 1.5mm) laying parallel with a spacing of 0.5mm between them.

2.4 Annealing

The last step in the fabrication process is the annealing. During this step the layers (with the aluminum contacts on top) were heated to 130°C for 30 minutes in a Thermo Scientific Oven. This is done to ensure a proper Ohmic connection between the aluminum contacts and the films, and to release internal stresses and impurities inside the contacts [22] [34].

3 Characterization process

This chapter describes the characterization process of the thin Ge(Sn):H films. The characterization process consists of various measurements to obtain material properties of the layers. The measurements done in this thesis were: Fourier transform infrared spectroscopy, Raman spectroscopy, spectroscopic ellipsometry, energy dispersive X-ray spectroscopy, photo conductivity and dark conductivity. The layers deposited on glass (containing the aluminum contacts) were used for the conductivity measurements and the layers on the Si wafers were used for the other measurements. By performing these measurements, there is sufficient information to know whether the material requirements, as described in the introduction, are met. In sections 3.1-3.5 their working principles will be explained.

3.1 Fourier transform infrared spectroscopy

Fourier transform infrared spectroscopy (FTIR) measures the absorption of the sample when an infrared light is perpendicular incident on it. In this thesis the Thermo Fisher Nicolet 5700 spectrometer was used to perform FTIR measurements. The wavenumber of the incident light varied between 400 and 4000cm^{-1}. The incident infrared light causes the atomic bonds to vibrate [34]. An atomic bond can vibrate in different ways, such as wagging, stretching and bending. These vibrational modes can lead to the absorption of the incident light. Absorption occurs when the frequency of the incident light equals the frequency of the vibration of the atomic bonds [23]. As the type of atomic bond and its vibration correspond to a certain wavenumber, it is possible to identify what type of bonds (and their type of vibration) are present inside the sample.

To obtain a FTIR spectrum, the following steps have to be carried out. First the thin layer deposited on the silicon wafer must be placed into the vacuum chamber together with a background material. The used background material was a blank silicon wafer without any deposition on it. Both substrates will be measured by the spectrometer and the final result is an absorption spectrum of the deposited layer that is corrected by the absorption spectrum of the blank silicon wafer. By using the Fityk freeware, a manually made baseline was subtracted from the FTIR spectrum to measure the area under the peaks. The area calculation is done by fitting Gaussian functions inside the peaks, and the area under these Gaussians were automatically calculated in the Fityk freeware.

An example of a Ge:H spectrum with subtracted baseline is given in figure 13 (in green). In figure 13, the type of bond is given per peak. As an example, the high peak around 560cm^{-1} corresponds to a (wagging) Ge-H bond. Other type of bonds present in this layer are Ge-C_x, Ge-O_x, Si-O_x and Si-H.

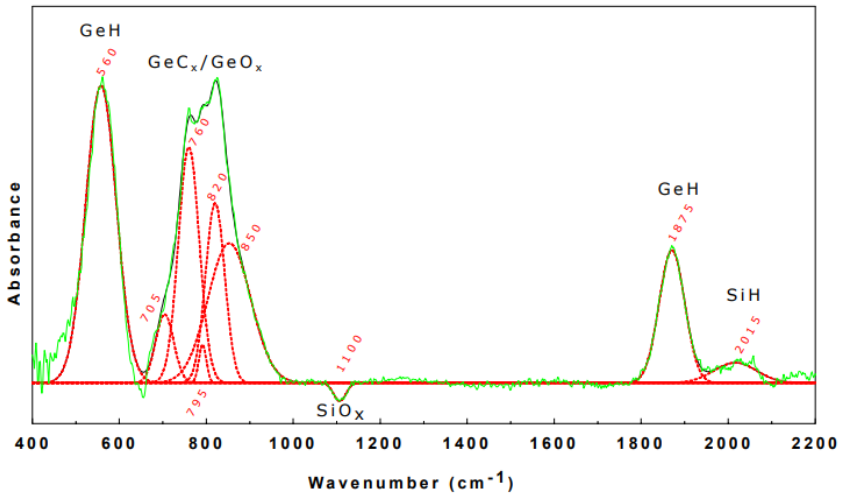

Figure 13: An example FTIR absorbance spectrum for an oxidized and carbonized Ge:H layer [22].

By determining the peak areas of the Gaussians (in red), several material characteristics can be obtained. One of the characteristics is the hydrogen concentration (C_H) inside the layers. The hydrogen concentration is determined by the Ge-H bond located around 560cm^{-1} and its calculation is given in equation 5.

$$C_H = \frac{N_H}{N_{Ge}} \cdot 100\% \tag{5}$$

In equation 5, N_H is the hydrogen content and N_{Ge} is the germanium content. For N_{Ge} the atomic density of germanium is used, which is 4.22x10^{22}cm^{-3} [22]. The hydrogen content was calculated by the following equation.

$$N_H = A\int\left(\frac{\alpha(\omega)}{\omega}\right)d\omega \approx \frac{A\cdot\ln(10)\cdot A_{560}}{d\cdot\omega_{560}} \tag{6}$$

Here, A is a proportionality constant of 1.3x10^{19}cm^{-2} [36], d the thickness of the deposition, A_{560} the area under the fitted Gaussian for the Ge-H bond at 560cm^{-1} and ω_{560} the wavenumber for the Ge-H bond which is automatically equal to 560cm^{-1}.

Another characteristic is the stability of the layer. For this, we are interested in the peaks located in the 700-1050cm^{-1} range. These peaks correspond to Ge-C$_x$ and Ge-O$_x$ bonds, indicating oxidation and carbonization of the material, which are indicative of an unstable material [37]. This instability is undesired because, amongst other reasons, it results in higher bandgaps. The absorption coefficient α_{tot} is used to indicate the degree of oxidation and carbonization of the material.

$$\alpha_{tot} = \alpha_{GeO_x} + \alpha_{GeC_x} \tag{7}$$

Where α_{GeOx} is the absorption coefficient of the Ge-O$_x$ bonds and α_{GeCx} the absorption coefficient of Ge-C$_x$ bonds. Both absorption coefficients can be calculated in a similar way:

$$\alpha_{GeO_x} = \frac{\ln(10)}{d} \cdot \sum \left(\frac{A_{GeO_x,n}(\omega)}{\omega_n} \right) \quad (8)$$

$$\alpha_{GeC_x} = \frac{\ln(10)}{d} \cdot \sum \left(\frac{A_{GeC_x,n}(\omega)}{\omega_n} \right) \quad (9)$$

Where $A_{GeOx,n}$ is the area under a Gaussian in the 800-1050cm^{-1} range, $A_{GeC,n}$ the area of a Gaussian in the 700-800cm^{-1} range and ω_n the wave number where the peak of the Gaussian is located. When a peak appears around 800cm^{-1}, it can be arbitrary if this corresponds to a Ge-O_x or a Ge-C_x bond. Therefore only α_{tot} will be discussed in the thesis.

The last characteristic that will be described is the ratio of the areas under the Gaussians located at 1875cm^{-1} (corresponding to a low stretching mode Ge-H bond) and 1980cm^{-1} (corresponding to a high stretching mode Ge-H bond). Parameter *R* is the area ratio of the peaks located at 1980cm^{-1} to 1875cm^{-1}.

3.2 Raman spectroscopy

Raman spectroscopy is based on the Raman Effect, which occurs when a monochromatic light scatters inelastic after it was incident on the film. In this work the Renishaw in-Via Raman Microscope containing a monochromatic argon laser with a wavelength of 514nm was used to perform the measurement. The scattered light has either the same frequency or a different frequency than the incident light. When the frequency is changed, the shift in frequency is called the Raman shift and the scattering is called Raman scattering [23]. It is called Rayleigh scattering if the frequency does not change.

By knowing the size in Raman shift, it is possible to identify materials and in our case: to determine the crystallinity of the deposited layer. The crystallinity tells whether the atom structure is amorphous or crystalline. Amorphous germanium has 4 distinct vibrational modes in the 80-280cm^{-1} range, while nano-crystalline germanium has shifts around 300cm^{-1}. Each shift size corresponds to another stretching mode of the atoms in the layer. The possible stretching modes are: transverse acoustic (TA) for 80cm^{-1}, longitudinal acoustic for 177cm^{-1}, longitudinal optic (LO) for 230cm^{-1} and transverse optic (TO) for 278cm^{-1} [31].

In the Raman spectrum a peak appears when these Raman shifts were detected and in each peak, except the TA as its wavenumber was located outside the measurement range, a Gaussian was fitted. For each fitted Gaussian the area was calculated. The crystallinity can then be calculated as follows.

$$X_C = \frac{I_{C-Ge}}{I_{C-Ge} + \gamma \cdot I_{a-Ge}} \quad (10)$$

Where $I_{C\text{-}Ge}$ is the area of the crystalline germanium peak, $I_{a\text{-}Ge}$ the area corresponding to the a-Ge TO mode and *y* (0.85) is a correction factor [31].

3.3 Spectroscopic ellipsometry

With the spectroscopic ellipsometry (SE) measurement multiple optical properties can be measured. In this project a J.A. Woollam M-2000 Ellipsometer was used to perform the SE measurements. To perform this measurement, the deposition can be processed on several types of substrates. The SE technique is based on the polarization change of a light beam when it is incident on the sample and when it reflects to the detector. During the interaction with the sample, the polarization changes from being linear to elliptical, as shown in figure 14.

The setup of the SE measurement is as follows: a light source emits a linearly polarized light on the sample and the reflected elliptically polarized light will be detected by a detector. The angle between the light source and the normal varied, between 55 and 70 degrees for glass substrates and between 65-75 degrees for silicon substrates, in steps of 5 degrees. Per step the SE setup measures the polarization change by finding the amplitude ratio and the phase difference of the p- and s-components of the reflective light. The amplitude ratio and the phase difference were measured for a wavelength range of 190 nm – 1700 nm.

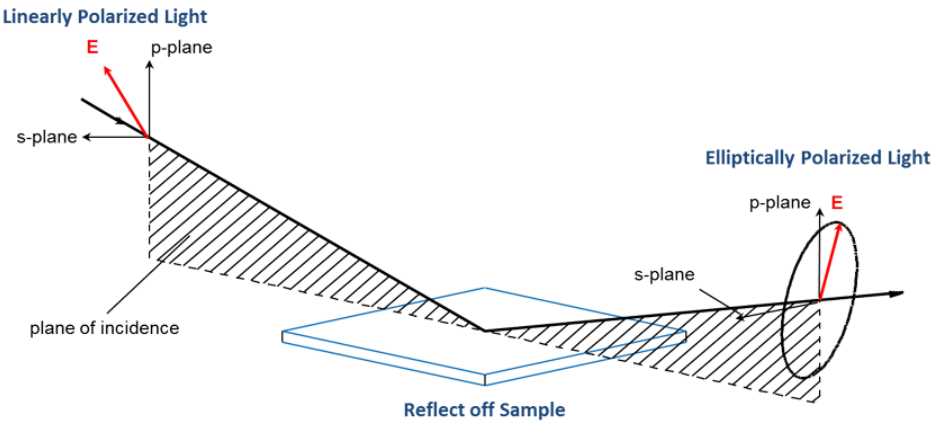

Figure 14: Schematic representation of the working principle of the SE setup [22]. Linearly polarized light hits the sample and reflects as elliptically polarized light to the detector.

The CompleteEase software was used to determine various optical material properties after performing the measurement. In the software a Cody Lorentz model was fit to the measurement data and its parameter values result, amongst others, in the following information about the material: film thickness, refractive index ($n_{@600nm}$), Tauc bandgap (E_{Tauc}) and the absorption coefficient per wavelength. Also the accuracy of the fitted model was given by the software. When the mean square error (MSE) of the fit reaches its lowest value below 10, the result was considered sufficiently accurate for the purpose of this research.

In this work, E_{Tauc} is not used as bandgap energy as the model is less reliable for heterogeneous materials. As an alternative, the optical bandgap energy E_{04} is calculated from the measurement data. This optical bandgap is determined by calculating the photon energy (see equation 1) at which the absorption coefficient equals 10^4 cm^{-1}. In previous works sometimes E_{03} was used as optical bandgap instead of E_{04}. However, in this work E_{03} was not always positioned inside the fitted wavelength range.

3.4 Energy dispersive x-ray spectroscopy

Energy dispersive x-ray spectroscopy (EDX) is a characterization technique used to determine the elemental composition of a sample. In this thesis the FEI Nova NanoSEM 450 was used for this type of measurement. Its working principle is based on X-ray excitation of the sample after it was bombarded by a beam of electrons [22]. As the measurement spot could be in the range of nm^2, a scanning electron microscope (SEM) was used to identify the desired area on the layer. The energy of the excited X-rays were measured by a detector and each energy level indicates another type of element. Next to this, the detector also counts the number of X-rays containing a specific energy level. Combining these data results in an EDX spectrum. An example EDX spectrum is shown in figure 15.

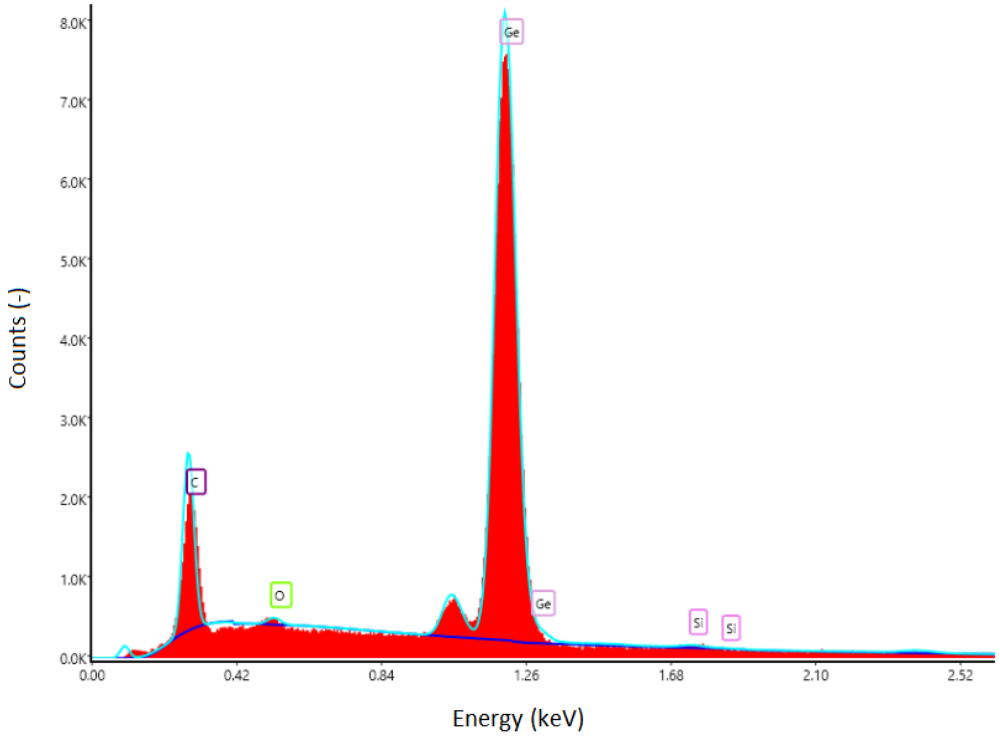

Figure 15: Example of an EDX spectrum.

3.5 Electrical conductivity

Electrical conductivity is a measure of how well/poor the deposited layer conducts a current. This depends on the mobility and concentration of the free charge carriers (electrons and holes), as shown in equation 11.

$$\sigma = e(\mu_e n + \mu_h p) \tag{11}$$

Where *e* is the elementary charge, μ the mobility and *n*/*p* the concentration of respectively electrons and holes. In this thesis, the conductivity was measured with and without illumination of a light source.

3.5.1 Photo conductivity

The photo conductivity is the conductivity of a material when it is illuminated. In this research a WACOM solar simulator was used as illumination source. The WACOM simulator uses halogen and xenon lamps to emit an AM1.5 spectrum. By emitting this spectrum, the layer heats up to 25°C and therefore the standard test conditions are met. Two probes were used to measure the current between the aluminum contacts when a voltage of 10V was applied. Then the photo conductivity can be calculated with the following equation:

$$\sigma_{photo} = \frac{I}{V \cdot b \cdot d} \tag{12}$$

Where *I* is the current corresponding with the voltage *V*, *b* the ratio of contact length (long side) and the distance between the two aluminum contacts (ratio is 40) and *d* the thickness of the deposited layer.

3.5.2 Dark conductivity and activation energy

The dark conductivity is the same type of measurement as the photo conductivity, but now the material is not illuminated. An anti-transparent hood is placed over the dark conductivity setup to create a dark environment. Similar as for the photo conductivity, two probes were used to measure the current for an applied voltage of 10V. Therefore the same equation (11) can be used as for the photo conductivity.

Next to the dark conductivity, also the activation energy can be measured by using the same setup. The activation energy is the difference between the Fermi level and the closest band (conduction or valence band). So an intrinsic material has an activation energy equal to half the bandgap energy. For performing an activation measurement, the samples were heated up between 60 and 130°C in steps of 5°C and per step the current was measured at an applied voltage of 10V. This measurement was done by a Keithley 6517B electrometer. Using these 15 measurement results, the activation energy can be known by rewriting equation 13 and calculate the slope of $\ln(\sigma_{dark})$ over $1/k_bT$.

$$\sigma_{dark}(T) = \sigma_0 \cdot e^{-\frac{E_{act}}{k_B T}} \tag{13}$$

This equation is also called the Arrhenius equation, where E_{act} is the activation energy, k_b the Boltzmann constant and *T* the temperature.

4 Results of the Ge:H series

In this chapter, the results of the characterization process are given regarding the Ge:H films. As mentioned in the introduction, we are looking for device quality Ge:H layers for integration as bottom cells in multi-junction devices. Device quality means having a low bandgap energy, relatively high photo response and being intrinsic (Fermi level halfway bandgap). Additionally, the material has to be chemically stable (no interaction with other elements influencing the material properties). In previous works it was demonstrated that the chemical stability improved with increasing substrate temperatures during deposition [22, 23, 38]. For this reason, an approach to produce device quality Ge:H layers is to use processing temperatures in the 250-300°C range. Three temperature series were processed in this thesis and the effect of substrate temperature on the material properties is discussed in section 4.1. Also the influence of layer thickness and hydrogen dilution were investigated. These results are presented in sections 4.2 and 4.3, respectively. In section 4.4, a reflection on the results is given.

4.1 Influence of substrate temperature on material properties

Earlier research [22, 23] into PECVD processed Ge:H absorber layers showed that using higher substrate temperatures led to more stable layers; the post-deposition oxidation and/or carbonization was significantly lower when a substrate temperature of 275°C was used instead of 200°C. Next to this, the films processed at the substrate temperature of 275°C had a relatively lower optical bandgap energy and higher activation energy. The photo response, however, did not improve by a temperature increase. As this research was very promising and only done at two different temperatures, a follow-up research is needed to understand the effect of substrate temperature on the material properties in more detail for the 250-300°C range. Therefore three Ge:H temperature series were processed in this thesis. The three series differ in deposition conditions and resulting in a porous nc-Ge:H series, a dense nc-Ge:H series and a dense a-Ge:H series. The used substrate temperatures are 250°C, 260°C, 270°C, 275°C, 280°C, 290°C and 300°C. Table 1 shows the used deposition conditions for the processing of these series. The results of these temperature series are plotted in figure 16.

Table 1: Deposition conditions of the three Ge:H temperature series processed in this thesis.

	Series 1: porous nc-Ge:H	**Series 2: dense nc-Ge:H**	**Series 3: dense a-Ge:H**
F_{H2} (sccm)	200	200	200
F_{GeH4} (sccm)	0.5	1	2
F_{H2}/F_{GeH4} (-)	400	200	100
p (mbar)	5	1	4
P_{RF} (W)	10	5	3
e_d (mm)	11.5	13.5	11.5
T_s (°C)	250-300	250-300	250-300

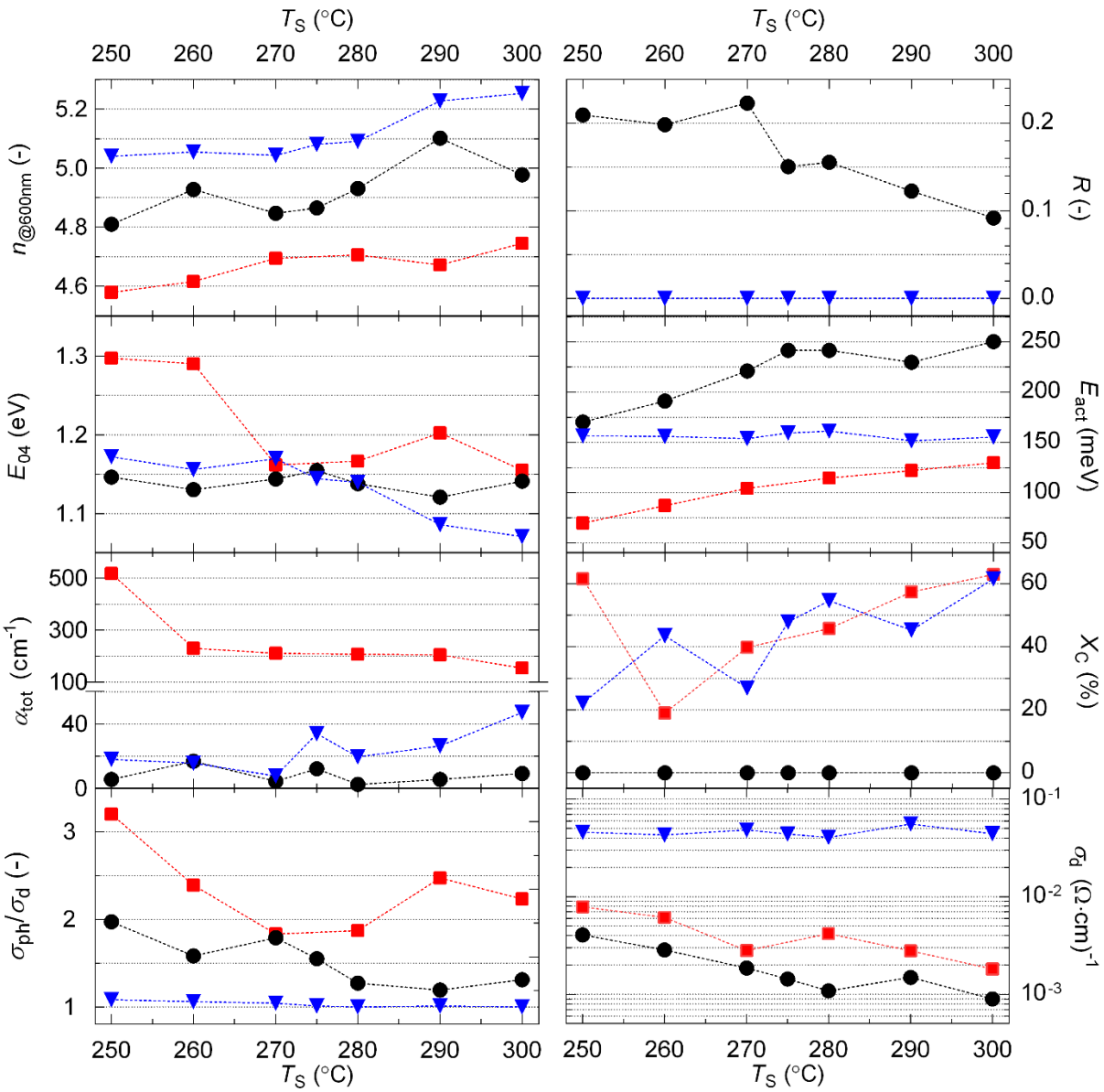

Figure 16: Three Ge:H temperature series processed in this thesis. The red squares correspond to porous nc-Ge:H, the blue triangles correspond to dense nc-Ge:H and the black circles correspond to dense a-Ge:H. The deposition conditions for each series is given in table 1.

Let us now take a closer look at the graphs in figure 16. In the top left corner, the refractive index ($n_{@600nm}$) is given. The refractive index can be used as a metric for the material density [31]. Therefore the porous nc-Ge:H series (red squares) contains lower refractive index values than the two dense series. From this refractive index graph, all three series show the same trend: the refractive index increases when a higher substrate temperature was used. For both nc-Ge:H series this trend is accompanied by an increase of the crystallinity (X_c). As crystalline phases are generally denser than amorphous phases, the increasing refractive index in combination with the crystallinity trend is not surprising. A result of the increasing refractive index trend is the reduction of the optical bandgap energy (E_{04}). For the porous nc-Ge:H series, however, the optical bandgap energy decrease could also be caused by the reduction in oxidation and/or carbonization (α_{tot}). Next to this, the lower α_{tot} also leads to higher activation energies (E_{act}) and lower dark conductivities (σ_{dark}) in the porous nc-Ge:H series. This has to do with the dominant defect type, which is for Ge:H further located from the conduction band edge than for GeO:H [31, 38-40].

In the dense nc-Ge:H series (blue triangles), both the dark conductivity and the activation energy are more or less constant over substrate temperature. So the defect density or dominant defect type plays no significant role here. Next to this, α_{tot} slightly increases when higher substrate temperatures were used. This trend is unexpected as earlier work showed the opposite result [38]. As the α_{tot} values are relatively low, it could be that the oxidation is limited to the surface of the films and did not reach the bulk.

The dense a-Ge:H series (black circles) also shows an increasing trend in densification when higher substrate temperatures were used. This trend cannot be explained by the crystallinity, because an amorphous material has a crystallinity of 0%. Next to this, α_{tot} is constant over substrate temperature and almost negligible. Therefore the explanation of the densification must be found in parameter *R*. As mentioned in chapter 3, *R* is the area ratio of the peaks located at 1980cm^{-1} (high stretching mode) and at 1875cm^{-1} (low stretching mode) in the FTIR spectrum. These high and low stretching mode Ge:H vibrations correspond to hydrogen atoms bonded to germanium atoms, where the hydrogen atoms are respectively located in nano-sized voids or smaller vacancies by the absence of germanium atoms [38]. The reduction in *R* therefore indicates a decrease in nano-sized voids, so there will be more germanium atoms per unit volume. As this is the definition of densification, the refractive index increases. The use of higher substrate temperatures also lead to higher activation energies and lower dark conductivities in the dense a-Ge:H series. The increasing activation energy in combination with the constant optical bandgap energy indicates a reduction of the n-type defect density. Next to this, parameter *R* decreases with increasing activation energy. So the n-type defect density is probably related to the concentration of large voids and small vacancies [38].

4.2 Influence of layer thickness on material properties

Two Ge:H thickness series were processed after requests from INTEL and Ghent University. The first series contains dense nc-Ge:H films and the second series is a dense a-Ge:H series. In earlier works [22, 23], the layer thickness was kept in the 100nm-150nm range. To understand the effect of layer thickness in more detail, this research contains films having thicknesses of 50nm, 100nm, 150nm, 200nm and 500nm. Table 2 shows the used deposition conditions for the processing of these series. The results of these thickness series are plotted in figure 17. Looking at these graphs, the trends are not as clear as in the previous temperature series. Nevertheless, the few trends that seems to be visible will be discussed below.

Table 2: Deposition conditions of the two Ge:H thickness series processed in this thesis.

	Series 1: dense nc-Ge:H	**Series 2: dense a-Ge:H**
F_{H2} (sccm)	200	200
F_{GeH4} (sccm)	1	2
F_{H2}/F_{GeH4} (-)	200	100
p (mbar)	1	4
P_{RF} (W)	5	3
e_d (mm)	13.5	11.5
T_s (°C)	290	290

From figure 17, the refractive index ($n_{@600nm}$) in the nc-Ge:H series (orange squares) shows a decreasing trend within the 50nm-200nm range, while the crystallinity (X_c) is more or less constant in the 75nm-200nm range. Also the oxidation and/or carbonization does not play a big role as α_{tot} is relatively low for all nc-Ge:H films. The reduced densification results in an increase of the optical bandgap energy (E_{04}). Next to this, the activation energy (E_{act}) increases and the dark conductivity (σ_{dark}) decreases as function of layer thickness. The last plain result of the nc-Ge:H series is the constant photo response ($\sigma_{photo}/\sigma_{dark}$), indicating a reduction in the photo conductivity as the dark conductivity decreases. The reductions in photo- and dark conductivity can be explained by the optical bandgap energy increase, what makes it more difficult for electrons to excite to the conduction band.

In contrast to the nc-Ge:H series, the refractive index in the a-Ge:H series (blue circles) shows an increasing trend. The increasing refractive index is not the result of crystallinity or oxidation/carbonization, because these films are amorphous and α_{tot} is relatively small. An explanation can also not be found in parameter R, as R does not show any trend. The increased densification did not result in an E_{04} change in this series. The last visible trend that can be seen is the reduction in dark conductivity.

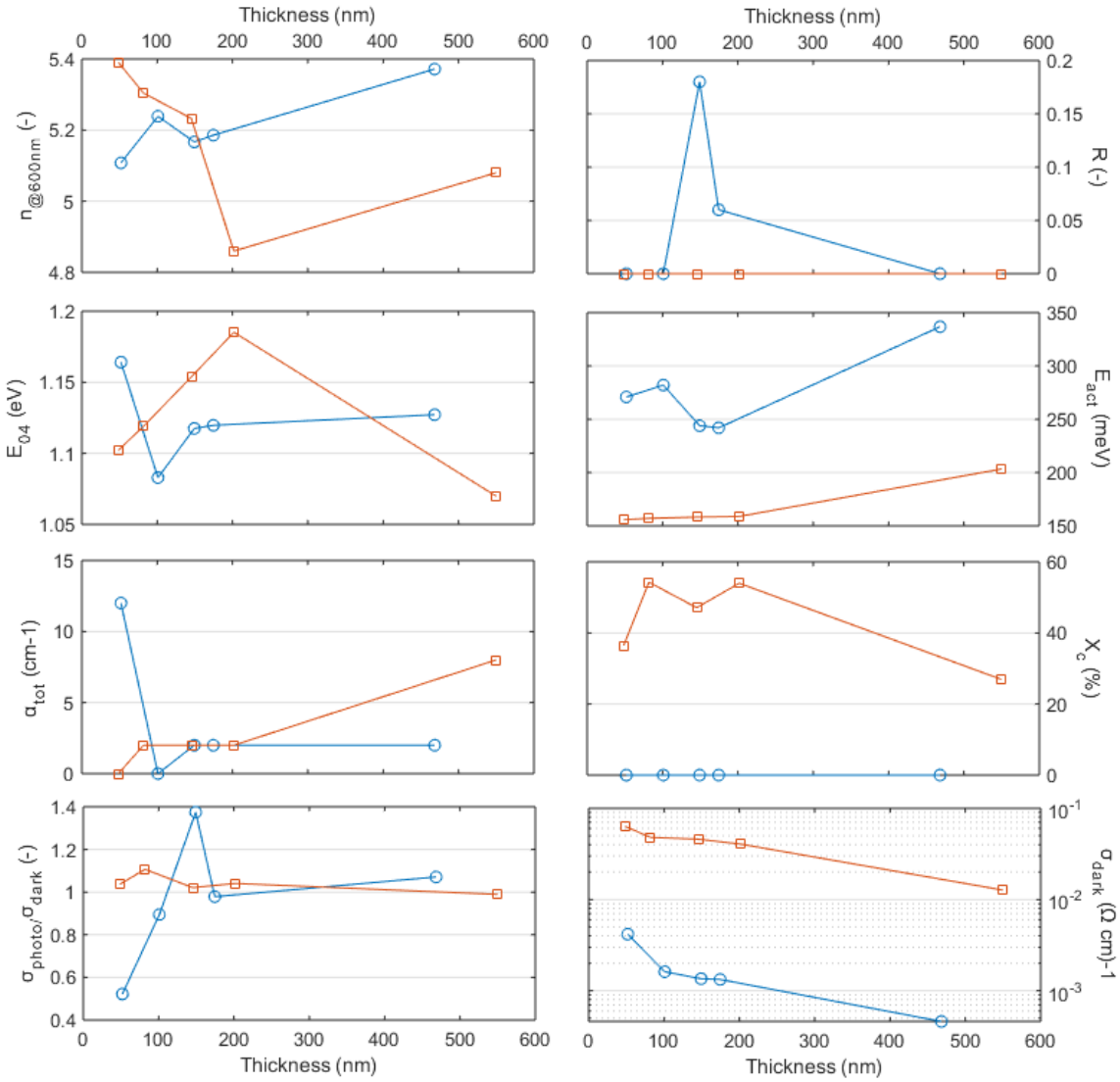

Figure 17: Two Ge:H thickness series processed in this thesis. The orange squares correspond to dense nc-Ge:H and the blue circles correspond to dense a-Ge:H. The deposition conditions for each series is given in table 2.

4.3 Influence of hydrogen dilution on material properties

Next to a temperature and a thickness series, also the influence of hydrogen dilution on the Ge:H material properties is investigated. The hydrogen dilution is the flow rate ratio of the hydrogen gas to the germane gas. An a-Ge:H series was processed containing the following hydrogen dilutions: 100, 200, 300 and 400. As this is a small series, the results presented in this section only give an indication of how the material properties could be influenced by the hydrogen dilution. Table 3 shows the used deposition conditions for the processing of these series. The results of these temperature series are plotted in figure 18. Figure 18 does not show a crystallinity graph as these layers were amorphous, what makes the crystallinity equal to zero. Again, not all graphs do show a clear trend. Therefore only the few visible trends will be discussed below.

Table 3: Deposition conditions of the Ge:H hydrogen dilution series processed in this thesis.

	Series 1: a-Ge:H
F_{H2} (sccm)	200
F_{GeH4} (sccm)	2, 1, 0.66, 0.5
F_{H2}/F_{GeH4} (-)	100, 200, 300, 400
p (mbar)	4
P_{RF} (W)	3
e_d (mm)	11.5
T_s (°C)	290

What immediately stands out in figure 18 is the growth rate graph, which shows a decreasing trend with increasing hydrogen dilution. This is an expected trend as a higher hydrogen dilution corresponds to a lower germanium share in the plasma, so less germanium radicals are present to grow the layer. Additionally, in hydrogen diluted plasmas, the growth rate is in competition with atomic hydrogen etching. Etching of the material increases when higher hydrogen dilutions are used. The layers become less dense when more hydrogen gas is added compared to germane gas, so the growth rate does not have a dominant effect on the material density. The decreasing trend in densification results in a higher optical bandgap energy (E_{04}).

In the activation energy (E_{act}) graph, the photo response ($\sigma_{photo}/\sigma_{dark}$) graph and the dark conductivity (σ_{dark}) graph, no clear trends are visible. The reason for this are the deviating results of the 100 hydrogen dilution layer. It is questionable why the results of this layer shows these adverse properties, because the oxidation and/or carbonization (α_{tot}) is minimal. Perhaps the condition of the plasma chamber was in a different state, as the 100 hydrogen dilution layer was processed several days earlier than the three others. Nevertheless, when we neglect the results of the 100 hydrogen dilution layer, the activation energy reduces and the dark conductivity increases as function of hydrogen dilution. This can be linked to the increased n-type defect density.

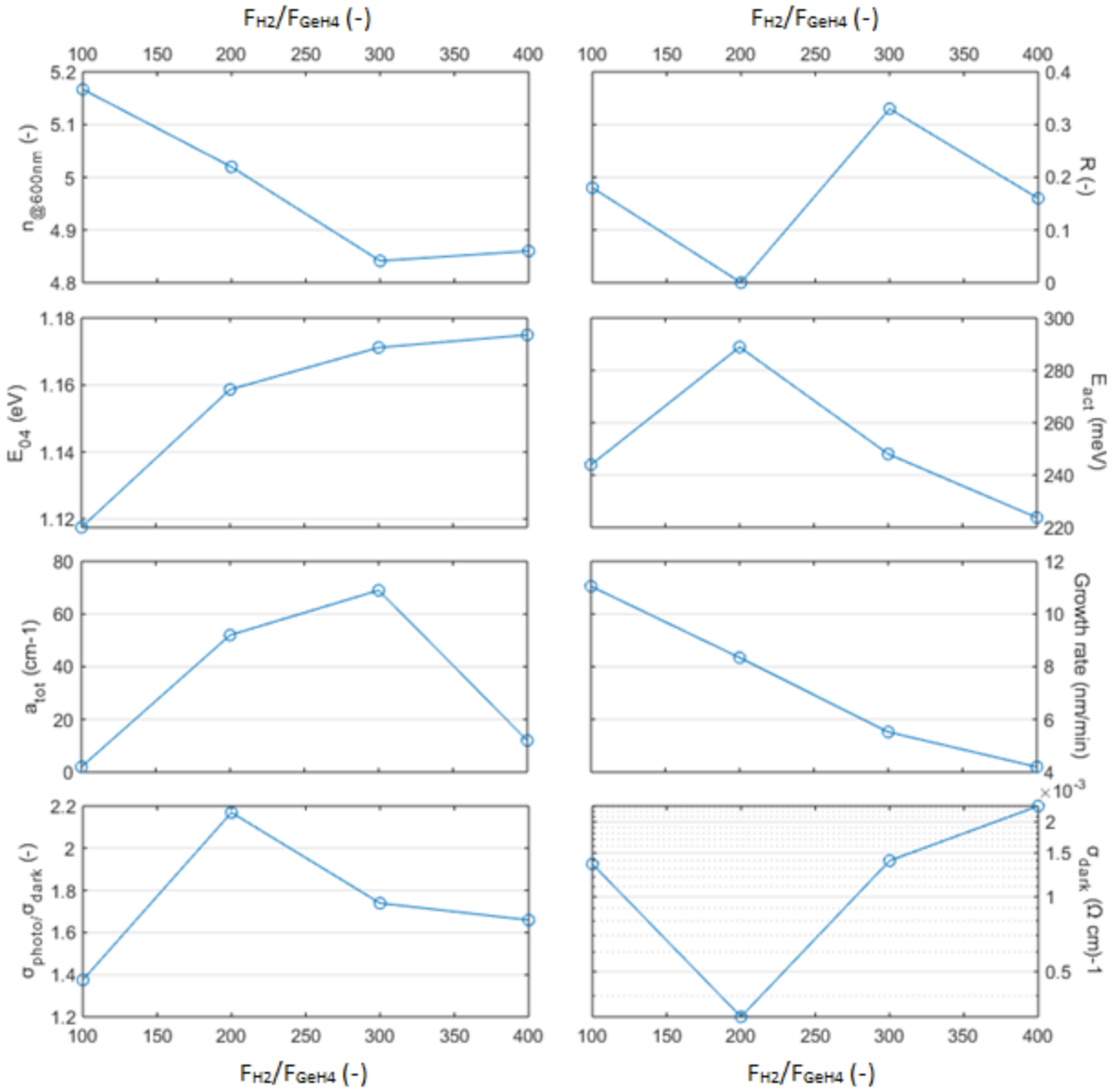

Figure 18: The a-Ge:H hydrogen dilution series processed in this thesis. The deposition conditions are given in table 3.

4.4 Reflection on the Ge:H results

After investigating the effects of several deposition parameters on the material properties of Ge:H, the following question can be answered: to what extend did we achieve device quality films? To answer this question, a comparison is made between the material requirements and the measured results. Next to this, the correlation between the deposition conditions and material properties will also be described.

First we consider the growth rate of the films. It was shown that the growth rate can be controlled by varying the hydrogen dilution. As a lower hydrogen dilution corresponds to a higher germanium share in the plasma, more germanium radicals are present to grow the layer. Additionally, etching of the material by hydrogen atoms also has an effect on the growth rate. In both cases, the growth rate of the films increases when lower hydrogen dilutions are used. Secondly, a way to regulate the optical bandgap energy to a more device quality material is by the use of higher substrate temperatures in the 250-300°C range. Also a decrease in hydrogen dilution (in the 100-400 range) led to films containing a lower optical bandgap energy. Low optical bandgap energies are generally accompanied by a densification of the material. For the amorphous Ge:H films, the highest refractive index ($n_{@600nm}$) we found was 5.37 and the lowest optical bandgap energy (E_{04}) was 1.08. For the nano-crystalline Ge:H films, the highest refractive index in this project was 5.39 and the lowest optical bandgap energy was 1.07eV. Theoretically, the bandgap energy of Ge:H could be 0.9eV [30]. Nevertheless, when we compare our values with literature, the $n_{@600nm}$ limit for Ge:H first was 5.25, and the limit of 1.07eV was also found in an earlier study [38]. When we consider the activation energy to know if the material is intrinsic, the dense a-Ge:H and the porous nc-Ge:H films became more intrinsic when higher substrate temperatures were used in the 250-300°C range. However, our processed films are clearly non-intrinsic as the activation energy is significantly lower than half the bandgap energy. The reason for this has to do with the defects inside the material, corresponding to hydrogen atoms located in nano-sized voids or smaller vacancies. For a-Ge:H and nc-Ge:H films, the highest activation energies we found were respectively 337meV and 203meV. When we compare our results with literature, the E_{act} limit for Ge:H films was 314meV [38]. The last material properties we consider are the photo response and the dark conductivity. The use of lower substrate temperatures resulted in the highest photo-responses because of the reduced chemical stability. However, the use of low substrate temperatures is not an option for obtaining device quality films as the post-deposition oxidation (and so the optical bandgap energy) will increase. Moreover, higher photo responses (above 4) were found in earlier works [22, 23]. The lowest dark conductivity in this work was about $5 \cdot 10^{-4}\ \Omega^{-1}cm^{-1}$ lower than found in literature [38].

After investigating the influence of substrate temperature, film thickness and hydrogen dilution on the material properties of Ge:H, a discussion can be given on what kind of conditions should be used to achieve device quality films. Using the highest substrate temperature in the 250-300°C range and the lowest hydrogen dilution in the 100-400 range gave us the most device quality a-Ge:H films. Next to this, the use of the highest substrate temperature in the 250-300°C range also resulted in the most device quality nc-Ge:H films. In the thickness series, a hydrogen dilution of 100 and a substrate temperature of 290°C were used, which are close to the recommended conditions. As a result, in this series we found a refractive index above 5.3, an optical bandgap energy below 1.1eV, an activation energy above 330meV and a dark conductivity below $5 \cdot 10^{-4}\ \Omega^{-1}cm^{-1}$. The photo response, however, did not improve when these conditions were used. Regarding the film thickness, the difference in material properties between films with thicknesses of 100nm and 200nm was relatively small. The most device quality films had a thickness of 500nm, although these results are less accurate.

5 Results of the GeSn:H series

In this chapter, the results of the characterization process are given regarding the GeSn:H films. As mentioned in the introduction, we are looking for device quality GeSn:H layers for integration as bottom cells in multi-junction devices. Device quality means having a low bandgap energy, relatively high photo response and being intrinsic (Fermi level halfway bandgap). As the amount of processed films is too small to generate conclusions, the results in this chapter only give a first indication of how the material properties could be influenced by the deposition parameters. The influence of several deposition parameters are investigated by processing a series for each. In total, the effect of the following parameters is investigated: duty cycle of the ALD valve, flow rate of helium as carrier gas, substrate temperature, hydrogen dilution, pressure and power. The results of these series are presented in sections 5.1–5.3. In section 5.4, a reflection on the results is given.

Before these series were processed, an experiment was performed into adding TMT in the plasma chamber during depositions of a-Ge:H. In this experiment, several a-GeSn:H layers were processed with different duty cycles and gas flows. After processing them, SEM pictures were made of the film surfaces and EDX measurements were performed. Three SEM pictures and a corresponding EDX spectrum are shown in figure 19. Figure 19 shows clusters of tin in the top-left SEM picture, so the tin particles are not uniformly distributed throughout the layer. By adding a helium carrier gas in the canister where the TMT is diluted, the tin clusters are still present but in another configuration. This can be seen in the top-right corner of figure 19. The EDX spectrum below shows that the 'white spots' in the SEM pictures indeed correspond to tin. This spectrum also shows a higher carbon peak compared to the tin peak for the (blue) area next to the tin cluster. This implies a relatively high carbon concentration inside the material, what could be the result of the relatively large amount of carbon added to the plasma when a TMT flow is introduced. To what extend the carbon has consequences on the material properties, can be seen in the next sections.

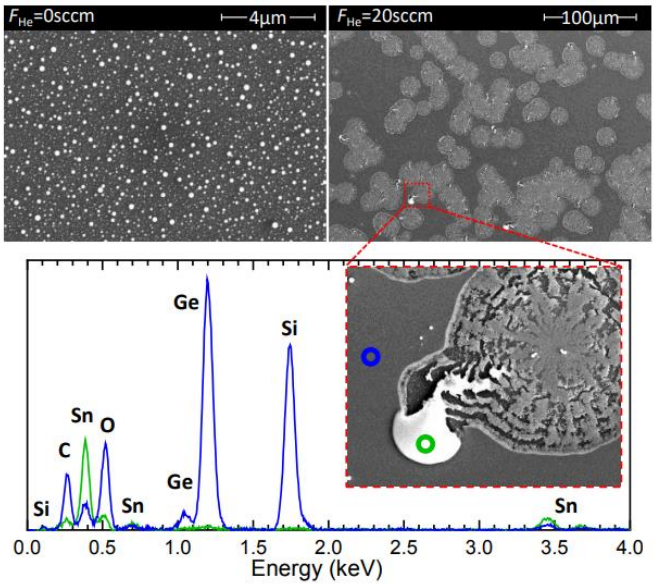

Figure 19: SEM images and an EDX spectrum of a-GeSn:H films. The helium flow is 0sccm in the top-left image and 20sccm in the top-right image. The EDX spectrum is given for both the tin cluster as the background surface.

5.1 Influence of TMT flow on material properties

In this section, the influence of TMT flow on the material properties of GeSn:H is investigated. As explained in chapter 2, the TMT flow is regulated by an ALD valve between the bubbler and the plasma chamber. One cycle of the ALD valve consists of an open time (in ms) plus a close time (in ms) and the amount of cycles depends on the processing time. In the three close time series, the following times are used: 5,000ms, 10,000ms, 20,000ms, 30,000ms, 40,000ms and 50,000ms. The open time series was processed containing the following times: 5ms, 6ms, 7ms and 8ms. Table 4 shows the deposition conditions used in these series. The results of the four open- and close time series are plotted in figure 20. From now on, the duty cycle will be used as an indication of the TMT flow. The duty cycle is the close time divided by the open time of the ALD valve, which means that a high duty cycle indicates a small amount of TMT injected into the plasma.

Table 4: Deposition conditions of the three GeSn:H close time series and the GeSn:H open time series processed in this thesis.

	Series 1: a-GeSn:H	**Series 2: a-GeSn:H**	**Series 3: nc-GeSn:H**	**Series 4: a-GeSn:H**
F_{H2} (sccm)	200	200	200	200
F_{GeH4} (sccm)	2	2	1	2
F_{H2}/F_{GeH4} (-)	100	100	200	100
F_{He} (sccm)	5	5	5	5
Open time per cycle (ms)	7	7	7	5-8
Close time per cycle (ms)	5,000-50,000	5,000-50,000	5,000-40,000	20,000
p (mbar)	4	4	1	4
P_{RF} (W)	3	3	5	3
e_d (mm)	11.5	11.5	13.5	11.5
T_s (°C)	210	270	290	230

From figure 20, the refractive index increases significantly for higher duty cycles. As a result, the optical bandgap energy (E_{04}) decreases with the duty cycle for all series except for the nc-GeSn:H samples (yellow triangles). Next to this, the three amorphous series also show decreasing trends in the activation energy (E_{act}) graph. The activation energy scales with the carbon fraction inside the material, as carbon passivates the defects in Ge:H. When less TMT is injected into the reaction chamber, the carbon fraction (and so the activation energy) is lower. The dark conductivity (σ_{dark}) increases when the activation energy decreases, resulting in higher photo responses ($\sigma_{photo}/\sigma_{dark}$) for lower duty cycles.

The results of the nano-crystalline series are somewhat different compared to the amorphous results. The optical bandgap energy and the activation energy both change as function of the duty cycle. Also the dark conductivity decreases. Elemental analysis performed by EDX measurements showed that these films contain relatively low atomic fractions of oxygen and carbon and a relatively high tin fraction. If we compare the raman shift of the c-Ge peak as a function of tin concentration in other works, as well as the overall crystallinity of our films, we can conclude that the tin concentration in the crystalline phase must be much higher than in the amorphous phase.

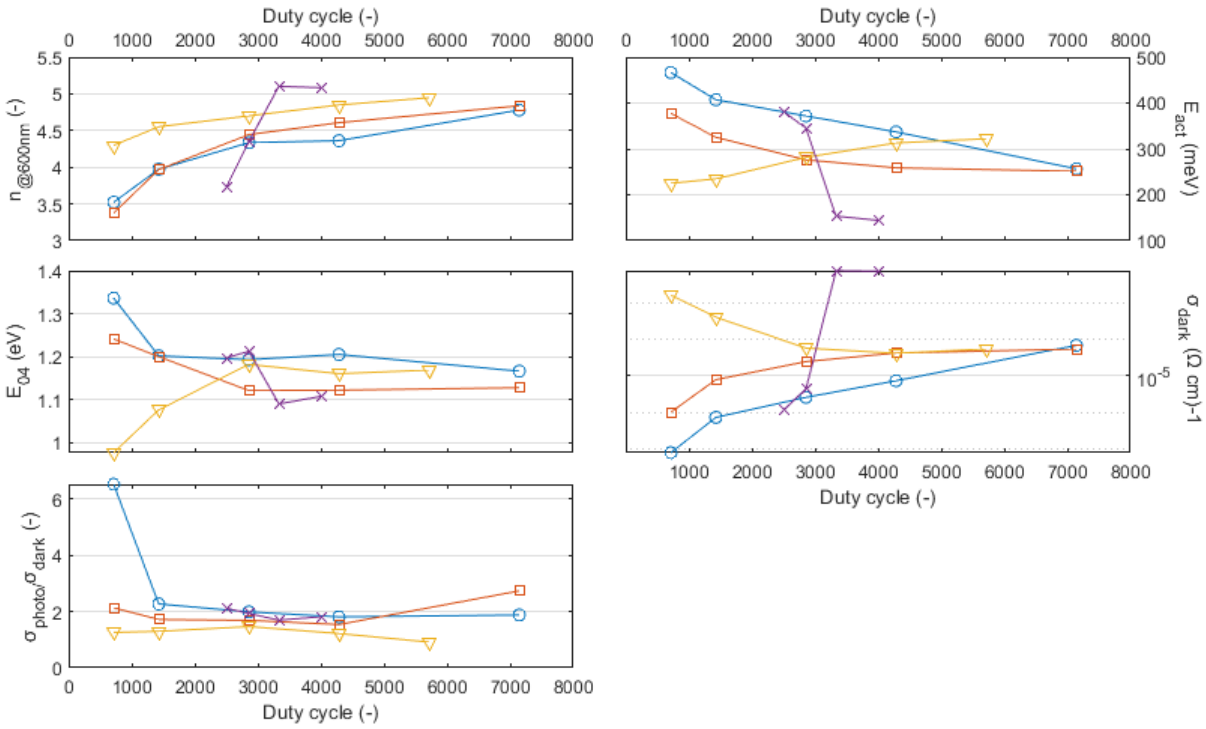

Figure 20: Four GeSn:H duty cycle series processed in this thesis. The blue circles correspond to series 1, the red squares correspond to series 2, the yellow triangles correspond to series 3 and the purple crosses correspond to series 4. The deposition conditions for each series is given in table 4.

The influence of the helium carrier gas flow on the material properties is also investigated. In figure 19, the tin clusters had another shape when the TMT was diluted in a helium gas before it was injected into the reaction chamber. However, it did not prevent the clustering. To check in more detail what the effect of the helium gas flow is on the material properties of the GeSn:H films, a series is processed containing the following helium gas flows: 0sccm, 10sccm, 30sccm and 50sccm. Table 5 shows the deposition conditions used in this series. The results are plotted in figure 21.

Table 5: Deposition conditions of the GeSn:H hydrogen dilution series processed in this thesis.

	Series 1: a-GeSn:H
F_{H2} (sccm)	200
F_{GeH4} (sccm)	2
F_{H2}/F_{GeH4} (-)	100
F_{He} (sccm)	0-50
Open time per cycle (ms)	7
Close time per cycle (ms)	20,000
p (mbar)	4
P_{RF} (W)	3
e_d (mm)	11.5
T_s (°C)	270

From the figure, the influence of the helium gas flow on the material properties is limited. The densification, dark conductivity and the photo response is more or less the same for all films. The optical bandgap energy, however, decreases when more helium gas is added. As the activation energy significantly higher for the 50sccm flow film, adding helium as carrier gas seems to be beneficial for obtaining device quality bottom cell absorber layers.

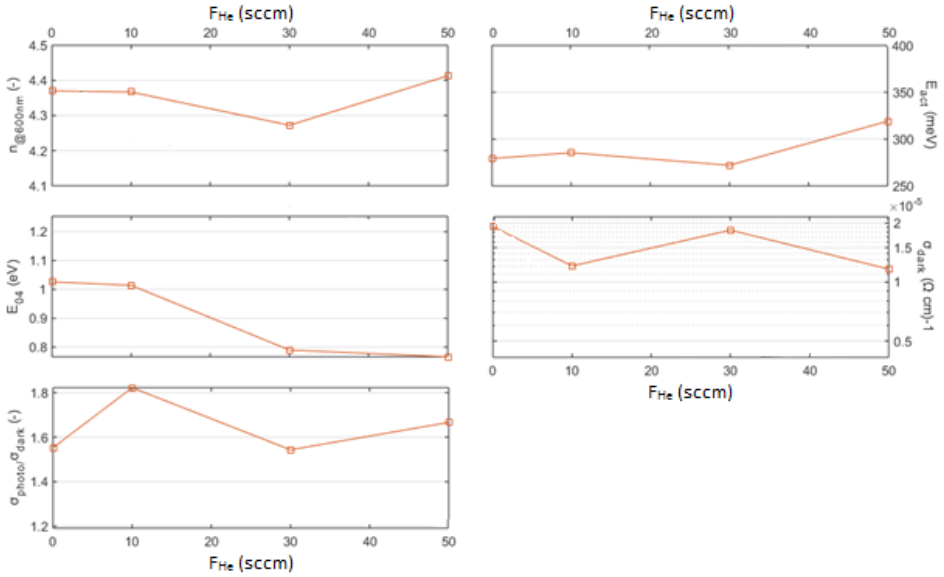

Figure 21: The a-GeSn:H helium (carrier) gas flow series processed in this thesis. The deposition conditions are given in table 5.

5.2 Influence of substrate temperature on material properties

In section 4.1, three substrate temperature series were shown regarding the Ge:H material. Increasing the substrate temperature up to 300°C resulted in denser films and a reduction of the optical bandgap energy. To check if the same trends hold for the GeSn:H material, again three substrate temperature series were processed. Table 6 shows the deposition conditions that were used to process these series. The open and close times were based on the results of the experiment described in section 5.1.

Table 6: Deposition conditions of the three a-GeSn:H substrate temperatures series processed in this thesis.

	Series 1	**Series 2**	**Series 3**
F_{H2} (sccm)	200	200	200
F_{GeH4} (sccm)	2	2	2
F_{H2}/F_{GeH4} (-)	100	100	100
F_{He} (sccm)	0	10	5
Open time per cycle (ms)	7	7	6
Close time per cycle (ms)	3,000	3,000	20,000
Duty cycle (-)	429	429	3333
p (mbar)	4	4	4
P_{RF} (W)	3	3	3
e_d (mm)	11.5	11.5	11.5
T_s (°C)	210-270	210-270	220-260

Before showing the results of the three substrate temperature series, we first take a closer look at the relation between the refractive index, optical bandgap energy and substrate temperature. In figure 22, the refractive index is plotted against the optical bandgap energy and the icon colour indicates the substrate temperature. The data of all GeSn:H films processed in this thesis is present in this graph. From the figure, the films processed with the highest substrate temperatures (above 270°C) generally contain a refractive index above 4.2 and an optical bandgap energy below 1.2eV. Using lower substrate temperatures can also result in lower refractive indexes or higher optical bandgap energies.

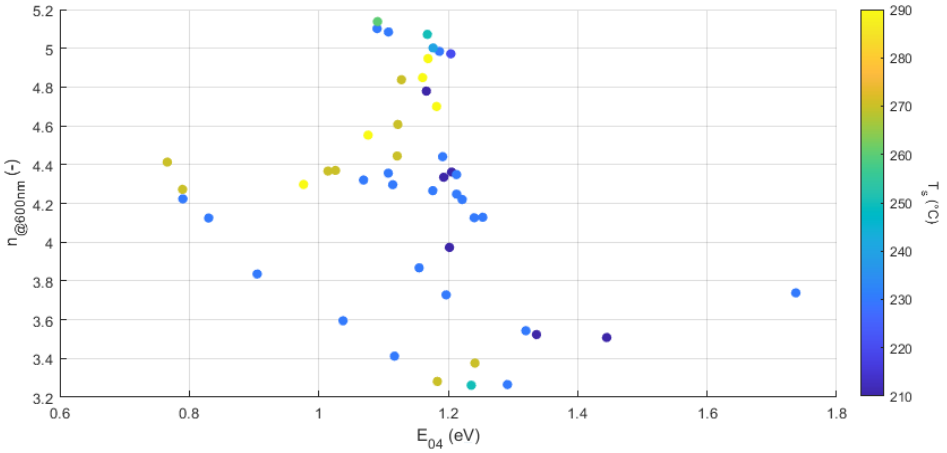

Figure 22: Plot of the refractive index against the optical bandgap energy containing all GeSn:H data gained in this thesis. The processing temperature is indicated by the icon colour.

The results of the three substrate temperature series are plotted in figure 23. First we consider series 1 (black circles) and series 2 (blue squares). These series differ in the helium gas flow rate. Similar as in section 5.1, the effect of the helium gas is limited. Nevertheless, the optical bandgap energy is somewhat lower and the activation energy a bit higher when the helium gas is added. However, this rule does not apply to a processing temperature of 270°C.

In figure 23, the refractive index is relatively low for the two series processed with low duty cycles compared to the series with the higher duty cycle. Therefore, the optical bandgap energy in series 3 is somewhat lower. Using higher substrate temperatures, what for Ge:H led to denser materials and lower bandgaps, does not result in denser films in the low duty cycle series. EDX measurements indicated a significant oxygen concentration in the low duty cycle series. For this reason, processing stable a-GeSn:H films could not be feasible when low duty cycles with TMT as a precursor are used. When we consider series 3, an increase in substrate temperature results in a densification of the film and a relatively low optical bandgap energy. From the EDX elemental analysis, the oxidation in this series reduces by the use of higher substrate temperature. As a result, the activation energy shows an increasing trend and the photo response decreases.

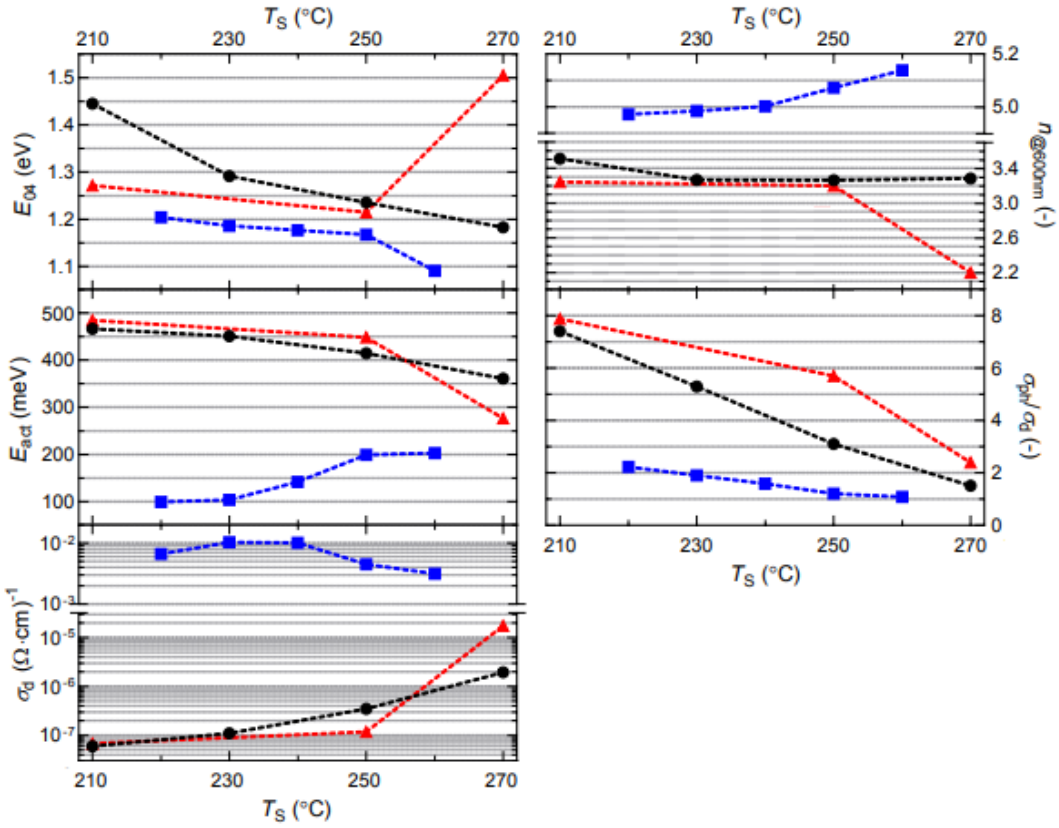

Figure 23: Three a-GeSn:H temperature series processed in this thesis. The black circles correspond to series 1, the red triangles correspond to series 2 and the blue squares correspond to series 3. The deposition conditions for each series is given in table 6.

5.3 Influence of hydrogen dilution, pressure and power on material properties

The last three a-GeSn:H series processed in this study are based on varying the hydrogen dilution, pressure and power. These series are processed at identical substrate temperatures, electrode distances and ALD valve settings, as shown in table 7. The used GeH_4 flows in the hydrogen dilution series are 0.5sccm, 0.75sccm, 1sccm, 1.5sccm, 2sccm, the used pressures in the pressure series are 1mbar, 2mbar, 3mbar, 4mbar and 5mbar and the used powers in the power series are 3W, 4W, 6W, 8W and 10W. Table 7 shows the deposition conditions that were used to process these series.

Table 7: Deposition conditions of the α-GeSn:H hydrogen dilution, pressure and power series processed in this thesis.

	Hydrogen dilution series	**Pressure series**	**Power series**
F_{H2} (sccm)	200	200	200
F_{GeH4} (sccm)	0.5-2	2	2
F_{H2}/F_{GeH4} (-)	100-400	100	100
F_{He} (sccm)	5	5	5
Open time per cycle (ms)	7	7	7
Close time per cycle (ms)	20,000	20,000	20,000
p (mbar)	4	1-5	4
P_{RF} (W)	3	3	3-10
e_d (mm)	11.5	11.5	11.5
T_s (°C)	230	230	230

In figures 24, 25 and 26 the results of respectively the hydrogen dilution, pressure and power series are plotted. We will first have a look at the results of the hydrogen dilution series in figure 24. Comparing the graphs in figure 24 to the hydrogen dilution graphs in the previous chapter, again the film growth rate reduces as a function of increasing hydrogen dilution. Therefore the same explanation can be given: a higher hydrogen dilution corresponds to a lower germanium share in the material and competition between growth rate and atomic hydrogen etching. The layers are denser when more germane gas is added in relation to hydrogen gas. The decreasing trend in densification results in a higher E_{04}. The photo response shows a decreasing trend while the dark conductivity is more or less constant.

Secondly, the results of the pressure series in figure 25 will be discussed. When low pressures are used, less precursor gas molecules are available in the reactor and the growth flux is decreased. This can be seen for the film processed with a pressure of 1 mbar. The relatively low growth rate of 0.6nm/min resulted in a film thickness of about 5nm. As such a low thickness generally leads to other material properties compared to films having thicknesses in the 60nm-100nm range, the results of the 1mbar layer will be neglected in this discussion. From figure 25, using pressures of 2-5mbar led to denser films. The optical bandgap energy graph, however, does not show a decreasing trend. It is unclear how the pressure influences the E_{04} based on this graph. An EDX measurement showed that the oxygen concentration decreases as function of pressure. This explains the significant increase in activation energy. The photo response graph shows a relatively small increase, while the dark conductivity remains constant.

Lastly, the influence of the power will be considered. In figure 26, the growth rate increases significantly when higher powers are used during the deposition. This was expected, because using higher powers indicates that more energy is added to the plasma, what lead to larger dissociation rates [34]. Using lower powers, however, results in a densification of the films. Therefore, the optical bandgap energy is the lowest for the films processed with 3W and 4W. Furthermore, the activation energy is a bit higher when a power of 3W or 4W is used, what makes the defect density the lowest for these two films. Next to this, the dark conductivity remains constant (when we neglect the outlier at 6W) and the photo response shows a decreasing trend, indicating a reduction in photo conductivity as function of power.

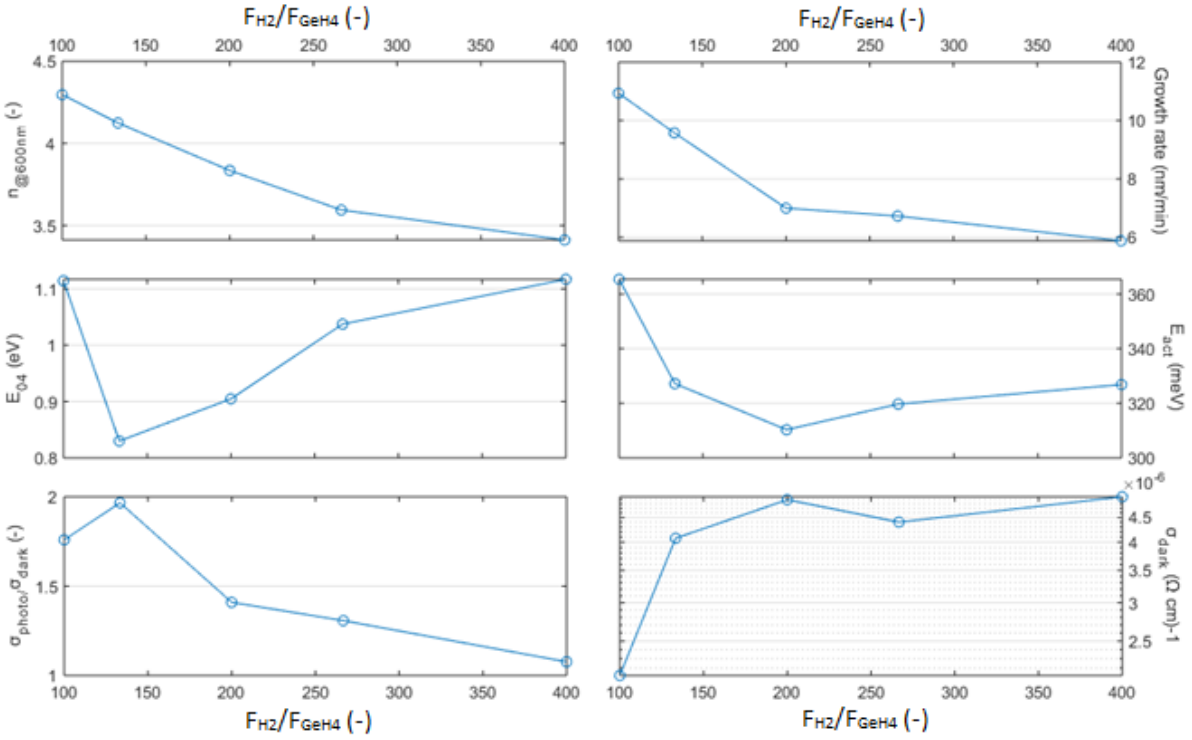

Figure 24: The a-GeSn:H hydrogen dilution series processed in this thesis. The deposition conditions are given in table 7.

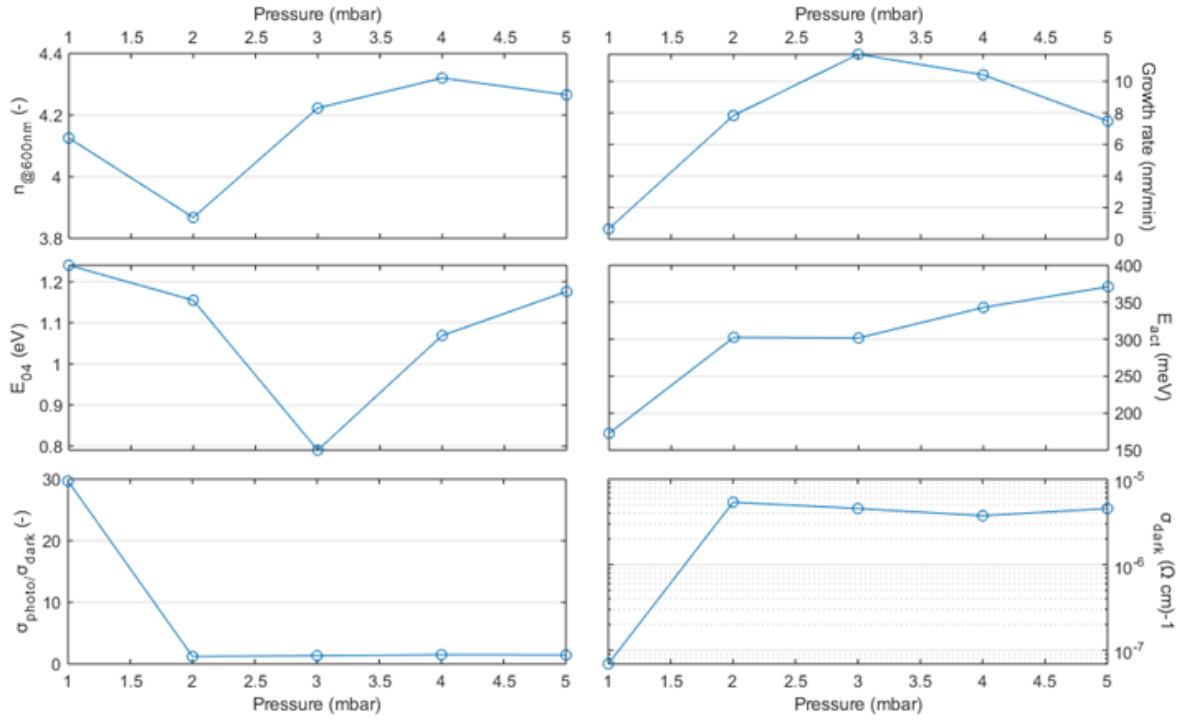

Figure 25: The a-GeSn:H pressure series processed in this thesis. The deposition conditions are given in table 7.

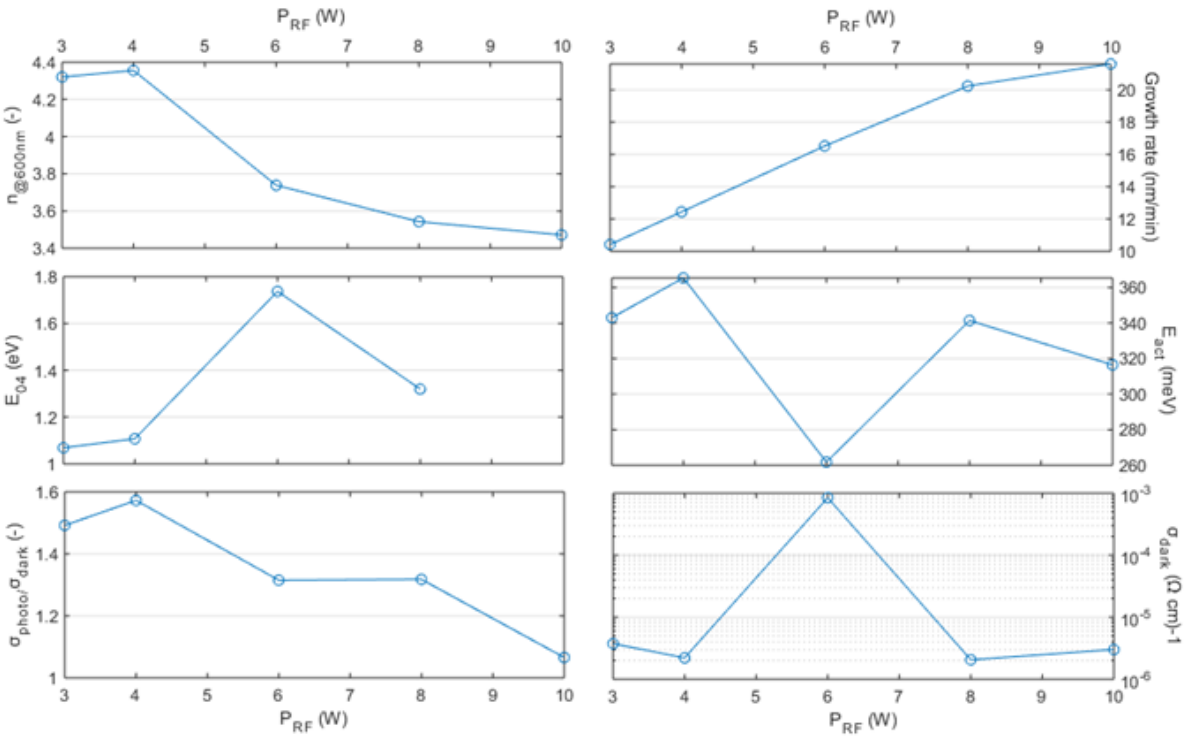

Figure 26: The a-GeSn:H power series processed in this thesis. The deposition conditions are given in table 5.

5.4 Reflection on the GeSn:H results

After investigating the effects of several deposition parameters on the material properties of GeSn:H, the following question can be answered: to what extend did we achieve device quality films? To answer this question, a comparison is made between the material requirements and the measured results. Next to this, the correlation between the deposition conditions and material properties will also be described below.

First we consider the growth rate of the films. Similar as for the Ge:H films, the growth rate of the GeSn:H films can be controlled by varying the hydrogen dilution. Next to this, the use of higher powers in the 3-10W range results in larger dissociation- and growth rates as more energy is added to the plasma. Secondly, the densification and bandgap energy of the a-GeSn:H films can be regulated to more device quality by increasing the substrate temperature (in the 200-300°C range) or by decreasing the hydrogen dilution (in the 100-400 range). There was also found that the lowest optical bandgap energies were achieved for relatively large Sn/C ratios. For the amorphous GeSn:H films, the highest refractive index ($n_{@600nm}$) we found was 5.14 and the lowest optical bandgap energy (E_{04}) was 0.77eV. For the nano-crystalline GeSn:H films, the highest refractive index in this project was 4.95 and the lowest optical bandgap energy was 0.98eV. The optical bandgap energies are closer to device quality compared with the Ge:H results. Thirdly, the activation energy changes by varying the duty cycle, substrate temperature, hydrogen dilution and/or pressure. Next to this, the activation energy scales with the carbon concentration inside the material. The highest activation energies we found were respectively 466meV and 322meV for a-GeSn:H and nc-GeSn:H. These values are significantly higher than for the Ge:H films. The last material properties we consider are the photo response and the dark conductivity. Lower substrate temperatures led to an increase of the photo response, but this condition is not an option for obtaining device quality films as the post-deposition oxidation will be larger. All other series did not show any trends regarding the photo response. The lowest dark conductivity was in the $10^{-8}\Omega^{-1}cm^{-1}$ range, what is a relatively large difference compared to the Ge:H results.

The results of the GeSn:H films are very promising in achieving device quality films. However, increasing the TMT supply/using lower duty cycles resulted in clusters of tin and significant oxygen and carbon concentrations throughout the layer. As a result, the a-GeSn:H films are less dense and the optical bandgap increases with increasing TMT flow. On the other hand, the amorphous layers became more intrinsic when lower duty cycles were applied. The activation energy scales with the carbon concentration inside the material as the carbon passivates the defects. A challenge is therefore to obtain denser films when higher amounts of TMT are injected into the reaction chamber. Managing the carbon, oxygen, germanium and tin fractions will be crucial for this. Lastly, adding helium as carrier gas can lead to lower bandgap energies and higher activation energies, although its influence was limited.

6 Conclusion

In this thesis, an investigation is done to develop the semiconductor materials Ge:H and GeSn:H using the PECVD technique. About 100 thin films were processed in the CASCADE reactor located in the Else Kooi Lab to optimize the plasma settings to deposit suitable thin films. After processing, all films were characterized by performing various measurements. Suitable Ge(Sn):H films could later be used as the absorber material in a bottom cell in multi-junction devices, provided they meet the device quality requirements: having a low bandgap energy to absorb photons in the higher wavelength range, being intrinsic for the use in a p-i-n junction and having a high enough photo response for obtaining a sufficient current density. Other than photovoltaic applications in where Ge or GeSn could be used are mid-infrared lasers, LED's or near-infrared light detectors [41-43]. The main question in this thesis is as follows:

How can the plasma settings be optimized to obtain PECVD processed device quality Ge(Sn):H films for the use as bottom cell absorber layers?

The answer on the main question is limited to the investigated area, which differs for both materials. For Ge:H the influence of substrate temperature, film thickness and hydrogen dilution was characterized, as shown in chapter 4. In chapter 5, the influence of duty cycle, helium carrier gas flow, hydrogen dilution temperature, pressure and power was investigated on the material properties of GeSn:H.

First we consider the Ge:H films processed in this work. An increase of substrate temperature (in the 250-300°C range) generally resulted in a densification of the films. The improved densification led to lower bandgap energies for both the nano-crystalline and amorphous films. Also a decrease in hydrogen dilution (in the 100-400 range) led to a-Ge:H films containing lower optical bandgap energies. Furthermore, the dense a-Ge:H and the porous nc-Ge:H films became more intrinsic when higher substrate temperatures were used in the 250-300°C range. Combining a substrate temperature of 290°C with a hydrogen dilution of 100, we processed promising a-Ge:H films containing a refractive index above 5.3, an optical bandgap energy below 1.1eV, an activation energy above 330meV and a dark conductivity below $5 \cdot 10^{-4}\ \Omega^{-1}cm^{-1}$. The photo response, however, did not improve when these conditions were used. Regarding the film thickness, the difference in material properties between films with thicknesses of 100nm and 200nm was relatively small. The most device quality films had a thickness of 500nm, although these results are less accurate.

Similar as for the Ge:H films, the densification and bandgap energy of the GeSn:H films can be regulated to more device quality by increasing the substrate temperature (in the 200-300°C range). Also a decrease in hydrogen dilution (in the 100-400 range) led to a-Ge:H films containing lower optical bandgap energies. There was found that the lowest optical bandgap energies were achieved for relatively large Sn/C ratios. The highest refractive index we found was 5.14 and the lowest optical bandgap energy was 0.77eV. For the nano-crystalline GeSn:H films, the highest refractive index and the lowest optical bandgap energy were respectively 4.95 and 0.98eV. The activation energy scales with the carbon concentration and can be regulated by the duty cycle, substrate temperature, hydrogen dilution and/or pressure. The highest activation energies in this project were respectively 466meV and 322meV for a-GeSn:H and nc-GeSn:H. These values are significantly higher than for the Ge:H films. The photo response was increased when lower substrate temperatures were used. However, these conditions are

not an option for obtaining device quality films as the post-deposition oxidation will be larger. The lowest dark conductivity was in the $10^{-8}\Omega^{-1}cm^{-1}$ range, what is a relatively large difference compared to the Ge:H results.

The results of the Ge(Sn):H films in this project are very promising in achieving device quality films, but still a lot of research needs to be done. Obtaining high photo responses for both materials is a challenging part for future research. Regarding GeSn:H, this material is in the early stage of research and still many other challenges are present. The major challenge in processing suitable GeSn:H films is to manage the atomic carbon, oxygen, germanium and tin fractions. When this can be achieved, the tin clusters and the significant oxygen and carbon concentrations throughout the layer could be prevented for relatively low duty cycles. Next to this, more research needs to be done into the influence of adding the helium carrier gas. It is still a bit doubtful whether the material properties really improve by adding helium as carrier gas. Finally, as TMT consists of carbon, it could be an option to use other gasses/liquids for adding tin into the plasma chamber.

References

1. Gilland, B., *Population, economic growth, and energy demand, 1985-2020.* Population and Development Review, 1988: p. 233-244.
2. IEA. *Data and statistics*. 2020 [cited 2020 28 Oct]; Available from: https://www.iea.org/data-and-statistics/data-tables?country=WORLD&energy=Balances&year=1990.
3. Ritchie, H. and M. Roser, *Energy.* Our World in Data, 2020.
4. IRENA, *Transforming the energy system - and holding the line on the rise of global temperatures*. 2019, Abu Dhabi.
5. IEA. *Data and statistics*. 2020 [cited 2020 29 Oct]; Available from: https://www.iea.org/data-and-statistics/data-browser?country=WORLD&fuel=Renewables%20and%20waste&indicator=SDG72modern.
6. Ritchie, H. and M. Roser, *Fossil fuels.* Our World in Data, 2017.
7. Kettell, S. *Oil crisis*. 2014 [cited 2020 3 Nov]; Available from: https://www.britannica.com/topic/oil-crisis.
8. Rapidtransition. *From oil crisis to energy revolution – how nations once before planned to kick the oil habit*. 2019 [cited 2020 3 Nov]; Available from: https://www.rapidtransition.org/stories/from-oil-crisis-to-energy-revolution-how-nations-once-before-planned-to-kick-the-oil-habit/.
9. Gade, M. *Half of plant and animal species at risk from climate change in world's most important natural places*. 2018 [cited 2020 3 Nov]; Available from: https://www.worldwildlife.org/press-releases/half-of-plant-and-animal-species-at-risk-from-climate-change-in-world-s-most-important-natural-places.
10. Rogelj, J., et al., *Paris Agreement climate proposals need a boost to keep warming well below 2 C.* Nature, 2016. **534**(7609): p. 631-639.
11. Commission, E. *2050 long-term strategy*. 2020 [cited 2020 13 Nov]; Available from: https://ec.europa.eu/clima/eu-action/climate-strategies-targets/2050-long-term-strategy_en.
12. Haque, A., *Electric Renewable Energy Systems*. 2016: Academic Press.
13. Di Zhang, A.A., *Design and Performance Optimization of Renewable Energy Systems*. 2021: Academic Press.
14. Perry, J. *In what part of the electromagnetic spectrum does the Sun emit energy?* 2020 [cited 2020 22 Nov]; Available from: https://astronomy.com/magazine/ask-astro/2020/07/in-what-part-of-the-spectrum-does-the-sun-emit-energy.
15. Smets, A.H., et al., *Solar Energy: The physics and engineering of photovoltaic conversion, technologies and systems*. 2015: UIT Cambridge.
16. Brownson, J. *Basic Rules of Light Quantification*. 2020 [cited 2020 22 Nov]; Available from: https://www.e-education.psu.edu/eme810/node/455.
17. Szantoi, Z., *Diagram of the light's electromagnetic spectrum, showing the different wavelengths of visible light*. 2013.
18. Kwarikunda, N. *Solar energy*. 2018 [cited 2020 3 Nov]; Available from: https://indico.cern.ch/event/656460/contributions/2750661/attachments/1686278/2711720/ASP2018_Solar_Energy_Lecture.pdf.
19. Young, A.T., *Air mass and refraction.* Applied optics, 1994. **33**(6): p. 1108-1110.
20. Halbleiter, *Fundamentals: Conductors – Insulators – Semiconductors* 2019.
21. Tulsani, H., *Differentiate between direct and indirect band gap semiconductors.* 2017.
22. Dingen, J.v., *Improving the stability and opto-electrical properties of hydrogenated amorphous and nano-crystalline germanium films*. 2021, Delft University of Technology: Delft. p. 10.

23. Roelandschap, P., *Development of device quality a-Ge:H absorber layers by Plasma Enhanced Chemical Vapor Deposition*. 2021, Delft University of Technology. p. 16.
24. Pinkse, J. and D. Van den Buuse, *The development and commercialization of solar PV technology in the oil industry.* Energy Policy, 2012. **40**: p. 11-20.
25. Green, M., *Recent developments in photovoltaics.* Solar energy, 2004. **76**(1-3): p. 3-8.
26. Ananthachar, V. *Current and next generation solar cell market outlook*. in *Proceedings of ISES World Congress 2007 (Vol. I–Vol. V)*. 2008. Springer.
27. Brown, G.F. and J. Wu, *Third generation photovoltaics.* Laser & Photonics Reviews, 2009. **3**(4): p. 394-405.
28. Hannah Ritchie, M.R., *Renewable Energy.* Our World in Data, 2020.
29. Boriskina, S.V. and G. Chen, *Exceeding the solar cell Shockley–Queisser limit via thermal up-conversion of low-energy photons.* Optics Communications, 2014. **314**: p. 71-78.
30. Thierry de Vrijer, A.S., *Thesis description Development of a novel low bandgap material based on a-GeSn:H* 2020, Delft University of Technology.
31. de Vrijer, T., et al., *The impact of processing conditions and post-deposition oxidation on the opto-electrical properties of hydrogenated amorphous and nano-crystalline Germanium films.* Journal of Non-Crystalline Solids, 2021. **553**: p. 120507.
32. Boenig, H., *Plasma science and technology*. 2019: Cornell University Press.
33. Thornton, J.A., *Plasma-assisted deposition processes: theory, mechanisms and applications.* Thin Solid Films, 1983. **107**(1): p. 3-19.
34. Bouazzata, B., *Development of a-/nc-Ge:H - Growth and characterization of a low bandgap material*. 2020, Delft University of Technology. p. 18.
35. Raúl J. Martín-Palma, A.L., *Engineered Biomimicry.* Elsevier, 2013: p. 383-398.
36. Abo-Ghazala, M. and S.A. Hazrny, *Hydrogen bonding in hydrogenated amorphous germanium.* Tsinghua Science and Technology, 2004. **9**(2): p. 177-180.
37. Paul, W., *Structural, optical and photoelectronic properties of improved PECVD a-Ge: H.* Journal of non-crystalline solids, 1991. **137**: p. 803-808.
38. de Vrijer, T., et al., *Improved PECVD processed hydrogenated germanium films through temperature induced densification.* Materials Science in Semiconductor Processing, 2022. **138**: p. 106285.
39. Moreno, M., et al., *Boron doping compensation of hydrogenated amorphous and polymorphous germanium thin films for infrared detection applications.* Thin solid films, 2013. **548**: p. 533-538.
40. Schröder, B., et al., *Influence of oxygen incorporation on the properties of magnetron sputtered hydrogenated amorphous germanium films.* Applied physics letters, 1993. **62**(16): p. 1961-1963.
41. Wirths, S., D. Buca, and S. Mantl, *Si–Ge–Sn alloys: From growth to applications.* Progress in crystal growth and characterization of materials, 2016. **62**(1): p. 1-39.
42. Zhou, Y., et al., *Systematic study of GeSn heterostructure-based light-emitting diodes towards mid-infrared applications.* Journal of Applied Physics, 2016. **120**(2): p. 023102.
43. Krause, M., et al., *Microcrystalline germanium photodetectors.* MRS Online Proceedings Library Archive, 2001. **664**.